

The Population of Giant Clumps in Simulated High- z Galaxies: In-situ and Ex-situ, Migration and Survival

Nir Mandelker¹, Avishai Dekel¹, Daniel Ceverino², Dylan Tweed¹, Christopher E. Moody³, Joel Primack³

¹*Racah Institute of Physics, The Hebrew University, Jerusalem 91904, Israel*

²*Grupo de Astrofísica, Universidad Autónoma de Madrid, Madrid E-28049, Spain*

³*Department of Physics, University of California, Santa Cruz, CA 95064, USA*

ABSTRACT

We study the properties of giant clumps and their radial gradients in high- z disc galaxies using AMR cosmological simulations. Our sample consists of 770 snapshots in the redshift range $z = 4 - 1$ from 29 galaxies that at $z = 2$ span the stellar mass range $(0.2 - 3) \times 10^{11} M_{\odot}$. Extended gas discs exist in 83% of the snapshots. Clumps are identified by gas density in 3D and their stellar and dark matter components are considered thereafter. While most of the overdensities are diffuse and elongated, 91% of their mass and 83% of their star-formation rate (SFR) are in compact round clumps. Nearly all galaxies have a central, massive bulge clump, while 70% of the discs show off-center clumps, 3-4 per galaxy. The fraction of clumpy discs peaks at intermediate disc masses. Clumps are divided based on dark-matter content into *in-situ* and *ex-situ*, originating from violent disc instability (VDI) and minor mergers respectively. 60% of the discs are in a VDI phase showing off-center *in-situ* clumps, which contribute 1-7% of the disc mass and 5-45% of its SFR. The *in-situ* clumps constitute 75% of the off-center clumps in terms of number and SFR but only half the mass, each clump containing on average 1% of the disc mass and 6% of its SFR. They have young stellar ages, 100–400 Myr, and high specific SFR (sSFR), $1 - 10 \text{ Gyr}^{-1}$. They exhibit gradients resulting from inward clump migration, where the inner clumps are somewhat more massive and older, with lower gas fraction and sSFR and higher metallicity. Similar observed gradients indicate that clumps survive outflows. The *ex-situ* clumps have stellar ages 0.5–3 Gyr and $\text{sSFR} \sim 0.1 - 2 \text{ Gyr}^{-1}$, and they exhibit weaker gradients. Massive clumps of old stars at large radii are likely *ex-situ* mergers, though half of them share the disc rotation.

Key words: cosmology — galaxies: evolution — galaxies: formation — galaxies: kinematics and dynamics — stars: formation

1 INTRODUCTION

The typical massive star-forming galaxies (SFGs) at high redshift are different from their counterparts at $z = 0$. While low-redshift discs like the Milky Way form stars quiescently with typical star-formation rates (SFRs) of a few $M_{\odot} \text{ yr}^{-1}$ (e.g. Brinchmann et al. 2004), the SFR in typical SFGs at $z \sim 2$ is on the order of $100 M_{\odot} \text{ yr}^{-1}$ (Genzel et al. 2006; Förster Schreiber et al. 2006; Elmegreen et al. 2007; Genzel et al. 2008; Stark et al. 2008). Many of the massive SFGs have been spectroscopically confirmed to be rotating discs, with baryonic masses of $\sim 10^{11} M_{\odot}$ within radii of $\sim 10 \text{ kpc}$ (Genzel et al. 2006; Shapiro et al. 2008; Förster Schreiber et al. 2009).

Their peak rotation velocities are $V \sim 150 - 250 \text{ km s}^{-1}$, and their one-dimensional velocity dispersions are $\sigma \sim 20 - 80 \text{ km s}^{-1}$, namely $V/\sigma \sim 2 - 7$, as opposed to $10 - 20$ in today's spiral galaxies (Elmegreen & Elmegreen 2005; Genzel et al. 2006; Förster Schreiber et al. 2006, 2009; Cresci et al. 2009). Their gas fractions, estimated from CO measurements, are in the range $0.2 - 0.8$ (Tacconi et al. 2008, 2010), much higher than the fractions of $0.05 - 0.1$ in today's discs (Saintonge et al. 2011). This is driven by the intense inflow of cold gas in narrow streams along the filaments of the cosmic web (e.g., Dekel et al. 2009a). Such a high gas fraction, combined with the high disc surface density that is imposed by the high density of the Universe at high redshift, lead to gravitational disc instability (Toomre

1964). Under such conditions, the instability involves giant clumps and it operates on short, orbital timescales (Dekel et al. 2009b, hereafter DSC09). It is therefore termed “violent” disk instability (VDI), as opposed to the slow, “secular” instability in today’s discs. The large fraction of SFGs among $z \sim 2$ galaxies (e.g. Elmegreen et al. 2007; Tacconi et al. 2008) suggests that this phase is long lived, on the order of one to a few Gyr, comparable to the age of the Universe at $z \sim 2$.

The massive high- z SFG discs tend to be broken into several giant clumps, each typically ~ 1 kpc in diameter and $\sim 10^9 M_\odot$ in mass, where a large fraction of the star formation occurs (Elmegreen & Elmegreen 2005; Förster Schreiber et al. 2006; Genzel et al. 2008; Förster Schreiber et al. 2011b; Guo et al. 2012; Wisnioski et al. 2012). Therefore, these discs were at some point referred to as “chain” or “clump-cluster” galaxies, depending on their orientation relative to the line of sight (Cowie et al. 1995; van den Bergh 1996; Elmegreen et al. 2004a,b, 2005). The clumps are observed in both rest-frame UV and rest-frame optical emission (Genzel et al. 2008; Förster Schreiber et al. 2009, 2011b), and they do not appear to be a bandshift artifact, in the sense that images of low redshift galaxies would not appear as clumpy if observed at high redshift with limited resolution and low S/N (Elmegreen et al. 2009). Scaled down versions of these giant clumps, with radii of only a few hundred pc but similarly high SFR surface densities, are observed in strongly lensed $\sim 10^{10} M_\odot$ disc galaxies at similar redshifts (Jones et al. 2010).

The gravitational fragmentation of a gas-rich turbulent disc has been addressed in idealized simulations of isolated galaxies (Noguchi 1999; Gammie 2001; Immeli et al. 2004a,b; Bournaud et al. 2007; Bournaud & Elmegreen 2009; Elmegreen et al. 2008; Hopkins et al. 2012) as well as in a cosmological context, either analytically (DSC09; Cacciato et al. 2012; Genel et al. 2012a), or via cosmological simulations (Agertz et al. 2009; Ceverino et al. 2010, 2012; Genel et al. 2012b). Toomre (1964) showed that a rotating disc becomes unstable to local gravitational collapse once the surface density of gas and “cold” stars (Σ) becomes large enough for self-gravity to overcome the stabilizing effects of pressure (represented here by a velocity dispersion, σ) and centrifugal forces (represented by the disc angular velocity, Ω). This happens when the Toomre parameter $Q \propto \sigma\Omega/\Sigma$ becomes smaller than a critical value of order unity, Q_c . The characteristic scale of fragmentation grows with the gas fraction of the system, which explains why the $z \sim 2$ giant clumps are so much larger than the low-redshift giant molecular clouds (GMCs).

During a VDI phase, the disc can maintain a self-regulated, marginally unstable steady state, with a high velocity dispersion that keeps $Q \sim Q_c$ (DSC09; Krumholz & Burkert 2010; Cacciato et al. 2012; Genel et al. 2012a; Forbes et al. 2012, 2014). During this phase, clumps of a few percent of the disc mass and $\sim 10\%$ of its radius are formed. The

perturbed disc induces angular momentum outflow and mass inflow towards the center, partly due to clump migration caused by torques, dynamical friction, and clump-clump interactions within the disc. In the high- z gas-rich discs, the timescale for these processes is fast - comparable to the orbital time at the disc edge (DSC09 and references therein). The gravitational energy gained by the inflow in the disc, possibly along with clumpy accretion and feedback from stars and supernovae drive turbulence which keeps the disc in a marginally unstable state (DSC09; Krumholz & Burkert 2010; Cacciato et al. 2012; Genel et al. 2012a). This inflow can contribute to the growth of a central bulge (Bournaud et al. 2007; DSC09) and may fuel AGN (Bournaud et al. 2011, 2012), in a way that may depend on the SFR in the disc and whether the clumps survive intact until they coalesce at the center. While the growing bulge and the transformation of gas to stars tend to stabilize the disc (Martig et al. 2009; Cacciato et al. 2012), the continuous input of gas from the cosmic streams ensures the high gas surface density needed to maintain VDI for cosmological times, till $z \sim 1$ (Dekel et al. 2009b; Cacciato et al. 2012; Forbes et al. 2014).

This simple theoretical framework, where most of the observed clumps are formed *in situ* in the discs by gravitational instability, has been confirmed in high-resolution zoom-in cosmological simulations (Agertz et al. 2009; Ceverino et al. 2010, 2012). These studies used AMR hydrodynamics to zoom in on halos of mass $M_v \sim 5 \times 10^{11} M_\odot$ at $z \sim 2.3$ and revealed discs of a few times $10^{10} M_\odot$ with bulges of comparable mass. These discs remain in a marginally unstable state for ~ 1 Gyr while continuously forming giant clumps of masses $10^8 - 10^9 M_\odot$.

In these simulations, which employ thermal energy driven feedback from stellar winds and supernovae, the clumps remain intact for 1 – 2 disc orbital times as they migrate towards the galactic center where they coalesce with the bulge. In previous work (Ceverino et al. 2012) we studied the internal kinematics of the clumps and found that they are in approximate Jeans equilibrium, supported mostly by rotation and partly by pressure against further gravitational collapse. In addition to the *in-situ* clumps, we found a few *ex-situ* clumps, which seem to have joined the disc as minor mergers. These clumps exhibited old stellar ages and low gas fractions, while appearing quite similar to the *in-situ* clumps in gas and stellar maps of the disc. From a limited sample of ~ 70 *in-situ* clumps, we estimated the mean stellar age of the clumps to be ~ 150 Myr and found an apparent trend where clumps seem younger and more gas rich near the disc edge, consistent with early indications by observations. This preliminary analysis is expanded upon in this work (§6).

Our main goal in this paper is to analyze the properties of the clumps in a much larger suite of cosmological simulations. Our motivation is to verify the hypothesis of VDI-generated clumps, and to try to distinguish between the population of clumps formed *in-situ* by VDI and the clumps that formed *ex-situ* as galaxies and came in as minor mergers.

Our second goal is to address whether the *in-situ* clumps survive stellar-feedback-driven outflows and remain intact during their migration to the bulge (Krumholz & Dekel 2010; Dekel & Krumholz 2013), or whether they disrupt on dynamical timescales by enhanced feedback (Murray et al. 2010). SPH cosmological simulations by Genel et al. (2012b) which employ an enhanced-outflow version of the phenomenological model of Oppenheimer & Davé (2006, 2008), pushed the effect of outflows to the extreme and caused clumps to disrupt on a dynamical timescale of ~ 50 Myr. Simillar results were obtained in isoltaed disc simulations by Hopkins et al. (2012), though these simulations also overestimate the strength of radiation pressure (see §7.1). This has consequences on the disc structure and the bulge growth.

The simulations studied in this paper employ the same recipees for star-formation and feedback as in Ceverino et al. (2012). Thus, the clumps survive intact for orbital timescales of ~ 250 Myr, typically caught in what seems to be internal dynamical equilibrium while they accrete mass during their migration to the center. This may or may not be more realistic than the scenario where clumps disrupt in a dynamical time, and reality likely lies somewhere in between. Our aim here is to study the long-lived clumps produced in these simulations, and come up with observable properties that may help distinguish between the two extreme scenarios. These include radial variation of clump properties within the disc in comparison with radial gradients in the diffuse inter-clump component. Future work incorporating simulations with stronger feedback and outflows (N. Mandelker et al. in preparation) will help sharpen these distinguishing features and determine the effect of feedback on VDI.

Using a suite of 29 galaxies in the redshift range $1 < z < 4$, we identify clumps as overdensities in the three-dimensional gas distribution in the disc, and then measure the clump stellar and dark matter components. By identifying the clumps in the gas component, we trace the perturbations that lead to clump formation, and also capture young clumps in their early stages of collapse and star formation. The gas distribution also serves as a proxy for the distribution of star formation and young stars, which is traced, for example, by H_α observations. By considering the associated stars, we facilitate a comparison to observed stellar clumps. We assemble in this way a statistical sample of nearly 2000 compact, spherical clumps. Within this sample, we distinguish between *in-situ* and *ex-situ* clumps and quantify their respective contributions to the total clump population as well as to the total disc mass and SFR. We collect statistics on the masses, SFRs, ages, gas fractions and metallicities of each clump population and use these to predict observables for distinguishing between *in-situ* and *ex-situ* clumps.

This paper is organized as follows: In §2 we briefly present the suite of simulations, introduce the galaxy sample and describe our method for defining the galactic disc and identifying the clumps. More details are provided in three apendices: §A elaborates on the simulation method, §B describes the disc

definition and §C outlines our clump finding algortim. §3 describes our method for classifying the clumps into compact-spherical clumps and diffuse-elongated ones, as well as the distinction between *in-situ*, *ex-situ* and *bulge* clumps. In §4 we discuss the statistics of the discs that host off-center clumps, and in particular those discs undergoing VDI. In §5 we address the distributions of various properties of the clumps. In §6 we discuss radial variations of these properties within the disc. In §7 we discuss our results, particularly their implication for clump survival, and compare to preliminary observations. In §8 we present our conclusions.

2 ANALYZING THE SIMULATIONS

2.1 The Cosmological Simulations

We use zoom-in hydro cosmological simulations of 29 galaxies whose virial masses at $z = 2$ are in the range $2 \times 10^{11} \leq M_v \leq 3 \times 10^{12} M_\odot$. All the simulations were evolved to redshifts $z \lesssim 2$ and several of them were evolved to redshift $z \sim 1$, with an AMR maximum resolution of $35 - 70$ pc at all times. They utilize the ART code (Kravtsov et al. 1997; Kravtsov 2003), which accurately follows the evolution of a gravitating N-body system and the Eulerian gas dynamics using an adaptive mesh. Beyond gravity and hydrodynamics, the code incorporates at the subgrid level many of the physical processes relevant for galaxy formation. These include gas cooling by atomic hydrogen and helium, metal and molecular hydrogen cooling, photoionization heating by a UV background with partial self-shielding, star formation, stellar mass loss, metal enrichment of the ISM and feedback from stellar winds and supernovae, implemented as local injections of thermal energy. Further details concerning the simulation method are provided in an appendix, §A, as well as in Ceverino & Klypin (2009), Ceverino et al. (2010), and Dekel et al. (2013).

The dark-matter halos were drawn from N-body simulations of the Λ CDM comsology with the WMAP5 parameters (§A), in a comoving cosmological box. They were selected to have a virial mass in a desired range at a target redshift $z = 1$ (a few at $z = 0$). The only other selection criterion was that they show no ongoing major merger at that target time, which eliminates less than 10% of the halos. Five of the galaxies, MW01-MW04 and SFG1 (see §A), have been studied in some detail in Ceverino et al. (2010, 2012), where they are referred to, respectively, as galaxies B, C, A, D and E, ordered by virial mass at $z = 2$. Further information about the simulated halos, including their virial properties at $z = 2$, target halo mass and final redshift can be found in §A.

2.2 The Galaxy Sample

We focus on the redshift range $1 \leq z \leq 4$ where we have a total of 772 snapshots among the 29 simulations. We note that the outputs were equally spaced in expansion

factor $a = (1 + z)^{-1}$, so they become denser in time at lower redshifts. The time spacing between consecutive snapshots is on the order of 100 – 200 Myr, which is roughly half an orbital time at the disc edge or 10 – 20 clump dynamical times. This means that the clumps can evolve significantly from snapshot to snapshot, even if they do not disrupt or complete their migration. Therefore, while consecutive snapshots from the same simulation are not truly independent of each other, we treat them as such in our analysis, noting that several clumps in fact survive for 2-3 snapshots.

Our purpose is to study giant clumps formed in extended discs undergoing VDI, so we begin by identifying the disc component of each galaxy, modelling the disc as a cylinder with radius R_d and half thickness H_d . The disc plane and dimensions are determined iteratively. The disc axis, \hat{z} , is defined by the angular momentum of cold gas ($T < 1.5 \times 10^4 \text{K}$), which on average accounts for $\sim 97\%$ of the total gas mass in the disc. The radius R_d is chosen to contain 85% of the cold gas mass in the galactic midplane out to 0.15 of the virial radius R_v , and the height H_d is defined so that 85% of the cold gas mass in a thicker cylinder, where both radius and height equal R_d , lies within $\pm H_d$ of the midplane. Further details can be found in §B.

All the gas contained within the final cylinder is considered part of the disc. An additional kinematic selection is applied to the stellar particles in order to separate the disc stars from the bulge stars. A star particle is assigned to the disc only if the z -component of its angular momentum j_z is higher than a fraction f_J of the maximum angular momentum for the same orbital energy, $j_{max} = m|v|r$. Here, m is the mass of the star particle, $|v|$ is the magnitude of its velocity and r is its cylindrical radial distance from the galactic center. We adopt as default $f_J = 0.7$ (Ceverino et al. 2010).

The disc SFR is obtained crudely by $M_*(< \Delta t) / \Delta t$, where $M_*(< \Delta t)$ is the mass in disc stars younger than Δt . We adopt $\Delta t = 30 \text{Myr}$, which is long enough to ensure good statistics and short enough to be comparable to the dynamical time and to keep the error of ignoring stellar mass loss small. The absolute values of the SFR as such should not be trusted to better than a factor of two, also given that an uncertainty at such a level is intrinsic to our current simulations (see below), but the ratio of SFRs between discs and between clumps should be more reliable.

In order to get a sense of the time evolution of one of our clumpy galaxies, Fig. 1 and Fig. 2 show a sequence of 30 snapshots of VL02 in the range $0.20 \leq a \leq 0.50$ ($4 \geq z \geq 1$), projected both face on and edge on. From $a = 0.32$ and on, we see an extended, clumpy disc with average dimensions $R_d = 9.2 \text{kpc}$ ($\sim 7\%$ of the average virial radius) and $H_d = 1.4 \text{kpc}$. During this phase, there are on average 8 off-center, compact, *in-situ* clumps in the disc.

Since discs undergoing VDI are typically extended and gas rich, we pick up for analysis the discs having $R_d \geq R_{min} = \max(2 \text{kpc}, 0.03R_v)$. This sample of discs comprises $\sim 83\%$ of the snapshots. At high redshifts,

$2.5 \leq z \leq 4$, there are 222 discs spanning $M_d \simeq 8 \times 10^8 - 7 \times 10^{10} M_\odot$, with a median mass of $1 \times 10^{10} M_\odot$. At intermediate redshifts, $1.5 \leq z < 2.5$, there are 270 discs with $M_d \simeq 4 \times 10^9 - 1 \times 10^{11} M_\odot$ and a median value of $4 \times 10^{10} M_\odot$. At low redshifts, $1 \leq z < 1.5$, there are 149 discs with $M_d \simeq 1 \times 10^{10} - 1 \times 10^{11} M_\odot$ and a median of $6 \times 10^{10} M_\odot$. Our discs thus span a similar mass range to typical observed SFGs at similar redshifts (Förster Schreiber et al. 2009, 2011a; Guo et al. 2012; Wuyts et al. 2012).

Previous studies using a subsample of these galaxies (Ceverino et al. 2010, 2012) have shown that they are fairly consistent with certain observed properties of galaxies in similar ranges of mass and redshift, such as the relation between SFR and stellar mass and the Tully-Fisher relation.

However, a significant caveat to the simulations used here relates to the implementation of feedback, which is limited to effective prescriptions for thermal feedback from stellar winds and supernovae and does not address radiative feedback or AGN feedback. The galactic mass outflow rate in our simulations is therefore only a fraction of the SFR, with mass loading factors ranging from zero to unity with an average of $\eta \sim 0.3$ at $0.5R_v$, not reproducing observed strong outflows with mass loading factors of unity and above (Steidel et al. 2010; Genzel et al. 2011; Dekel & Krumholz 2013). The code also assumes a somewhat high SFR efficiency per free-fall time and does not follow in detail the formation of molecules and the effect of metallicity on the SFR (Krumholz & Dekel 2012). Therefore, the early SFR is overestimated, while the suppression of SFR in small galaxies is underestimated, resulting in excessive early star formation prior to $z \sim 3$, by a factor of order 2. This causes the typical gas fractions and SFRs at $z \sim 2$ to be underestimated by a factor of ~ 2 compared to observations of SFGs (Ceverino et al. 2010; Tacconi et al. 2010; Daddi et al. 2010). Furthermore, the fairly weak outflows lead to a stellar fraction of ~ 0.1 within the virial radius, a factor of 2-3 higher than the observationally indicated value (Pérez-González et al. 2008; Guo et al. 2010; Moster et al. 2010, 2013; Behroozi et al. 2013).

These inaccuracies in the SFR, feedback and outflows induce a limitation on the generality of our analysis, while the low gas fractions suggest that our simulations may conservatively underestimate the effects of gravitational instability in real galaxies at these redshifts. However, while precise numerical values for the gas fractions and SFR in our simulated galaxies should not be trusted to within a factor of 2, the relative trends we detect between the galaxies and between the clumps contained within them are likely to be at least qualitatively representative. These simulations offer the additional advantage of allowing us to examine VDI in the weak (but non-zero) feedback limit, as the first step in a broader study which will include simulations with stronger radiative feedback (N. Mandelker et al., in preparation) in order to study its effect on VDI.

A further consequence of the limited feedback is an underestimate of outflows from clumps compared to observations (Genzel et al. 2011; Newman et al.

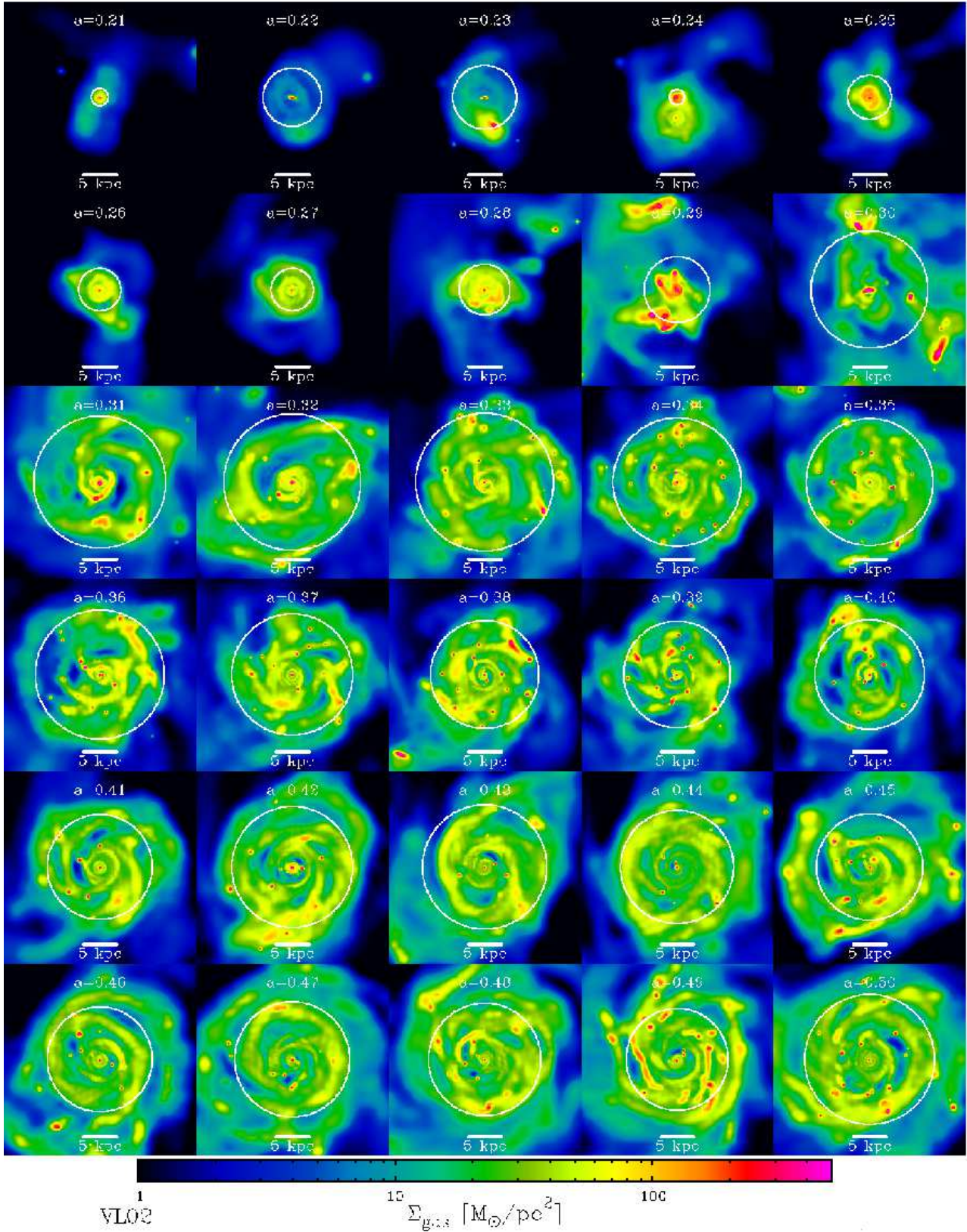


Figure 1. Evolution of gas density in galaxy VL02 between $z = 4$ and $z = 1$, face on views. The panels correspond to those shown in edge on projection in Fig. 2, and the x axis is the same. The expansion factor a is marked at the top of each panel. Color represents gas surface density according to the color bar. The disc radius R_d is marked by a white circle. The box shown is ± 15 kpc in each of the three directions. During several Gyr, the gas in this galaxy is an extended disc showing large-scale perturbations and giant compact clumps.

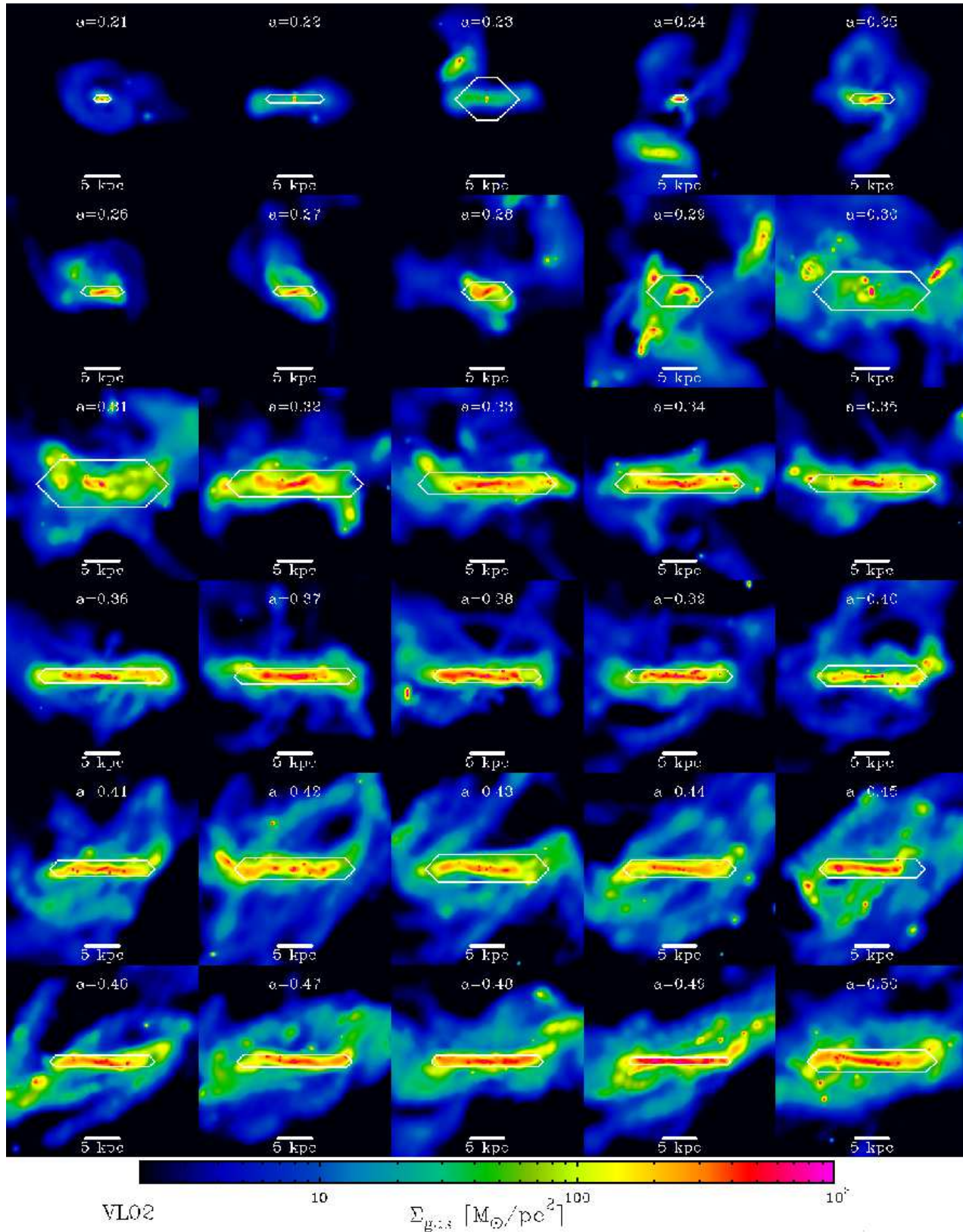


Figure 2. Evolution of gas density in galaxy VL02 between $z = 4$ and $z = 1$, edge on views. The panels correspond to those shown in face on projection in Fig. 1, and the x axis is the same. The expansion factor a is marked at the top of each panel. Color represents gas surface density according to the color bar. The disc boundaries are marked by a white line. The box shown is ± 15 kpc in each of the three directions. The disc is perturbed, often showing extended arms above and below the midplane.

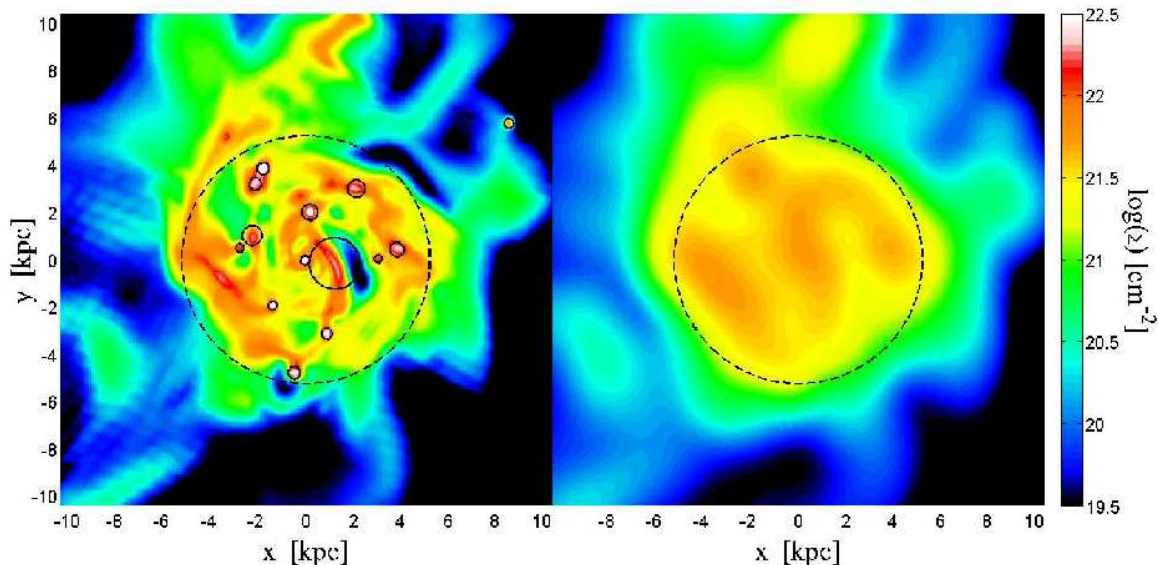


Figure 3. Clump identification. Shown is the gas surface density in a face-on view of MW3 at $a = 0.30$ ($z \simeq 2.33$). The disc radius, $R_d = 5.3$ kpc, is marked by a dashed circle. The scale of the image is $\pm 2R_d$ and the integration depth is $\pm 2H_d$, where $H_d = 1.1$ kpc. **Right:** The large-scale surface density of the background disc as obtained by broad Gaussian filtering of the 3D density prior to projection. **Left:** The small-scale density as obtained by smoothing with a narrow Gaussian filter, comparable to the simulation resolution scale. The identified clumps are marked by circles with radii equal to the clumps' 3D radii. The clumps identified by the automatic algorithm coincide with the visual identification.

2012), which may artificially extend clump lifetimes. However, as it is far from clear whether more realistic feedback can cause disruption of the massive clumps (Dekel & Krumholz 2013, see discussion in §7.1), our simulations have the advantage of allowing us to test the extreme scenario of long lived clumps and to compare to an extreme scenario where clumps are rapidly disrupted. Preliminary analysis of new simulations with non-thermal radiative feedback (Ceverino et al. 2014; Renaud et al. 2013) reveals that winds with realistic mass loading factors of $\eta \gtrsim 1$ do not alter the frequency of massive clumps with $\log(M_c) \gtrsim 8.5$ (Bournaud et al. 2014; Moody et al. 2014; N. Mandelker et al., in preparation; A. Dekel, F. Bournaud and N. Mandelker, in preparation).

2.3 The Clump Finder

We identify clumps in the 3D gas distribution in and around the disc. Warps near the edge of the disc, such as those visible in Fig. 2 at late times, can make it difficult to properly define the disc boundaries. A lot of material in these warps likely does belong to the disc, despite being outside the defined cylinder. For this reason, we also probe a larger volume for clumps, and envision an *extended disc*, with radius $2R_d$ and height $2H_d$. We assign gas and stars to it using analogous criteria to those described above for the original, slim disc. This extended volume also allows us to identify additional *ex-situ* clumps above and below the disc plane. When comparing clump properties such as mass or SFR to those of their host disc, we refer exclusively to the

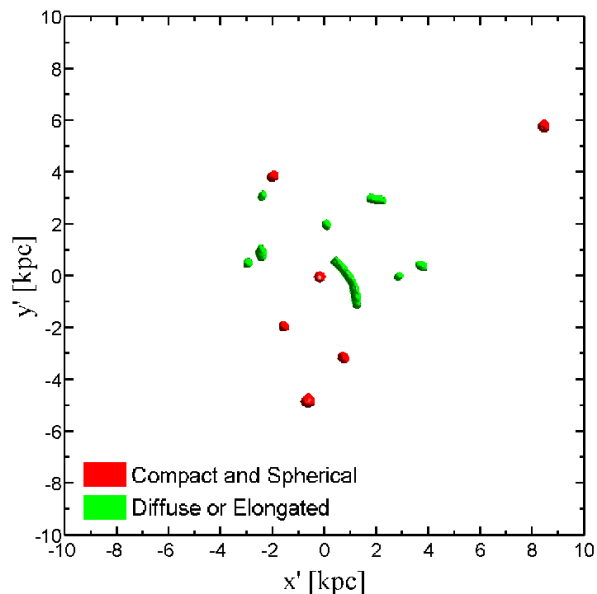


Figure 4. Clump identification. Face on projection of all cells in the 3D grid having density residuals above our adopted threshold. The 14 identified clumps, corresponding to the circles in Fig. 3, are visible. Compact, round clumps are colored red while diffuse or elongated clumps are colored green (see discussion in §3). The clumps identified by the automatic algorithm coincide with the visual identification.

extended disc, though the difference is small since 85% of the cold gas is already contained in the slim disc.

We briefly present here the main features of our

clump finder. A more complete discussion can be found in appendix §C. We smooth the 3D gas density field on two scales, first with a narrow Gaussian filter whose FWHM is taken to be 140 pc, comparable to the spatial resolution of the simulation, then with a wide Gaussian filter whose FWHM is taken to be 2 kpc, that will wash out features significantly smaller than the disc scale. We compute the residual density, and group together neighbouring cells above a threshold value. The local density peak defines the group center and each group is assigned a radius of a sphere that contains 90% of its total mass. We eliminate all groups with volumes smaller than $(140 \text{ pc})^3$. Stellar and dark matter particles are placed on the same grid and we then eliminate all groups whose baryonic masses are less than $10^{-4} M_{\text{d}}$. All the remaining groups make up our sample of clumps. In practice, as can be seen in Fig. 10, all compact clumps used in our analysis have masses larger than $\sim 10^{-3} M_{\text{d}}$.

This process is illustrated in Fig. 3 and Fig. 4 for one of the galaxies in our sample, MW3 at $a = 0.30$ or $z \simeq 2.33$, shown as well in Fig. B2. In Fig. 3 we plot the face-on surface density of the smoothed 3D gas density fields. The left panel relates to the narrow Gaussian which only washes out noise at the resolution level. Fourteen identified clumps have been marked. The apparently unidentified clump at $(x, y) \simeq (-3.5, 5)$ kpc is partly outside our volume, as can be seen in edge-on projections (Fig. B2) and was therefore ignored. The right panel relates to the wide Gaussian, which washes out features below the disc scale and leaves a good approximation for the local background in the disc. Figure 4 shows a face-on projection of the 3D residuals, after removing cells below the threshold and eliminating groups below the mass or volume limit. The identified clumps correspond to the circles in Fig. 3.

We note that the simulation resolution imposes an effective minimum mass for clumps, a crude estimate of which is as follows. With the smallest cell size being $35 - 70$ pc, and requiring as an absolute minimum at least 2^3 cells per clump, the minimum clump volume is $(140 \text{ pc})^3$. Assuming a mean gas density of 30 cm^{-3} within the clump (§A, §C and Fig. 5), the minimum clump gas mass is $M_{\text{gas},c}^{\text{min}} \gtrsim 10^{6.5} M_{\odot}$. With a typical gas fraction for *in-situ* clumps of 10% (Fig. 10), the minimum resolved baryonic mass in clumps is $M_{\text{c}}^{\text{min}} \sim 10^{7.5} M_{\odot}$. This minimum mass may vary with position in the disc and among different clumps as the disc density, the clump density contrast and the gas fraction may vary, and as the minimum cell size may be larger at the low-density regions in the outskirts of the disc.

3 CLASSIFICATION OF CLUMPS

In this section we detail how the clumps are classified based on their density (compact or diffuse), shape (round or elongated), position in the disc (central or off-center) and origin (*in-situ* or *ex-situ*). The classification is summarized schematically at the end of the section, in Fig. 8.

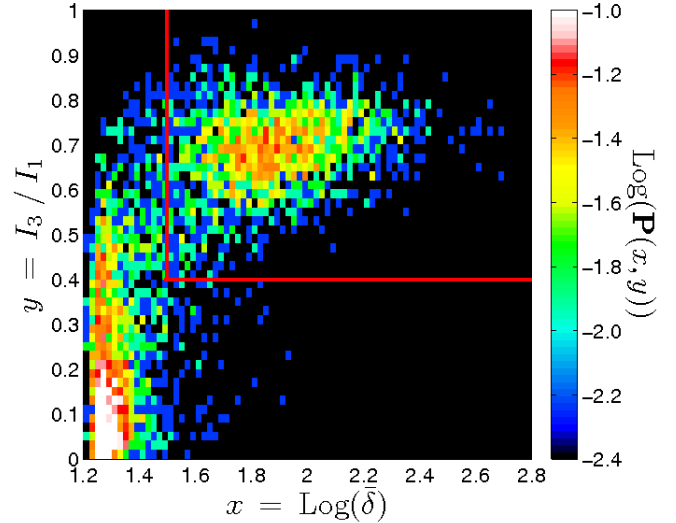


Figure 5. Clump density and shape. Shown is the 2D probability density in the $\log(\delta_{\rho}) - I_3/I_1$ plane for our population of clumps. There is a bi-modality between compact, oblate clumps (top right) and diffuse, elongated ones (bottom left). *Compact* clumps are defined by $\log(\delta_{\rho}) \geq 1.5$ and $I_3/I_1 \geq 0.4$.

3.1 Density and Shape

We identify over 4000 clumps in our sample of 641 discs. Taken at face value, this gives an average of over 6 clumps per disc in the entire redshift range $1 < z < 4$. However, not all the identified clumps represent observed clumps. For example, the elongated “worm-like” clump visible in Fig. 4 just to the right of the center (colored green) is clearly a different phenomenon than the smaller, rounder clumps visible in the same figure (colored red). Comparing to Fig. 3, we can see that this extended clump is part of a large-scale perturbation, perhaps indicative of the more linear phase of Toomre instability, before it is either disrupted by disc shear or stellar feedback, or collapses into smaller, rounder, denser clumps. Furthermore, a large fraction of the clumps in our sample are too small to be detected with the limited observational resolution.

One expects the VDI perturbations in the disc to eventually collapse into non-linear, self-gravitating, bound, spheroidal objects supported by rotation and pressure (e.g. DSC09; Bournaud et al. 2007; Krumholz & Dekel 2010; Genzel et al. 2011; Ceverino et al. 2012). We therefore wish to separate the compact clumps in our sample from more diffuse or elongated perturbations in the disc. For each clump, we measure its mean density residual $\bar{\delta}_{\rho}$ (see §C for the precise definition of the density residual δ) and the 3 eigenvalues of its inertia tensor $I_1 \geq I_2 \geq I_3$, computed from the unsmoothed gas density field in the region corresponding to the clump’s location. We use as a shape parameter the ratio of minimum to maximum eigenvalue I_3/I_1 , such that a value of 1 corresponds to a perfect sphere while a value of 0 corresponds to a 1D filament. An oblate rotating

clump, as predicted by Ceverino et al. (2012), will have $I_3/I_1 \simeq 0.5$.

Figure 5 shows the probability density in the plane defined by $x \equiv \log(\delta_\rho)$ and $y \equiv I_3/I_1$, $P(x, y)$. The probability for a clump to have values in an interval Δx about x and Δy about y is $P(x, y)\Delta x\Delta y$. There is a striking bimodality between a population of *compact*, oblate and rather round clumps centered at $(x, y) \sim (1.85, 0.70)$ and another population of diffuse, elongated clumps centered at $\sim (1.30, 0.05)$. We hereafter define a clump as *compact* if it has $x > 1.5$ and $y > 0.4$.

There are ~ 1850 *compact* clumps making up $\sim 46\%$ of the sample. However, they contain $\sim 91\%$ of the mass and $\sim 83\%$ of the star formation of the entire clump population, and so are of much greater interest. Throughout the remainder of our current analysis, we focus solely on these *compact* spheroidal clumps.

3.2 In-situ, Ex-situ and Bulge Clumps

3.2.1 Bulge clumps

As can be seen in Fig. 1 to Fig. 4, there is almost always a gas clump located at the disc center. We refer to these as *bulge* clumps, defined as clumps whose centers are within 1 resolution element of the disc center. We identify a compact *bulge* clump in $\gtrsim 91\%$ of the discs (and a diffuse *bulge* clump in an additional $\gtrsim 8\%$). These are always the most massive clumps in their host disc, often by more than an order of magnitude, and have the highest SFR, though relatively low sSFR (§5). The existence of such central clumps is not surprising, given that the disc center coincides with the peak of gas density, and that there is continuous gas inflow within the disc toward its center, driven either by VDI or by mergers (Dekel & Burkert 2014, A. Zolotov et al., in preparation).

Note that a bulge clump does not comprise the entire bulge — it is limited to the bulge central region. Recall that we first identify clumps in gas, not stars, so the sizes and masses of the *bulge* clumps are likely much smaller than those of the corresponding galactic bulges. On the other hand, since they do correspond to the peak of gas density within the bulge, it is not unreasonable to assume that the SFR in these clumps is indicative of the total SFR in our simulated bulges.

3.2.2 In-situ and Ex-situ off-center clumps

In addition to the *bulge* clumps, $\sim 70\%$ of the discs in our sample contain off-center clumps. There are two possible origins for an off-center clump: *in-situ* or *ex-situ*. *In-situ* clumps form during VDI from gas and cold stars within the disc, in regions where $Q \lesssim 1$. They are expected to bind only small amounts of dark matter, because the dissipationless dark-matter particles are "hot", with large and rather isotropic velocity dispersions, preventing them from participating in the disc instability which is driven by the cold gas and stars in the disc. *Ex-situ* clumps, on the other hand, merged in as external galaxies with their own gas, stars and dark matter components.

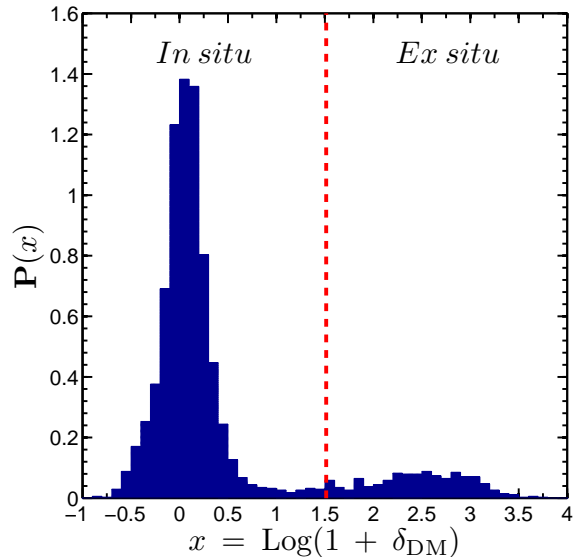


Figure 6. *In-situ* vs *Ex-situ* clumps. Probability density of $x \equiv \log(1 + \delta_{\text{DM}})$ for all *off-center* clumps in our sample. A bi-modality is evident, and we define *ex-situ* clumps as having $x \geq 1.5$.

The distinction between *in-situ* and *ex-situ* clumps is important because it will allow us to ascertain the relative contributions of internal instabilities and mergers to various phenomena, such as disc morphology, bulge growth and SFR. In addition, correlations between properties of *in-situ* clumps and between them and their host discs, especially those that are not expected for *ex-situ* clumps, will offer insight into the nature of VDI and clump evolution.

Our major criterion for distinguishing between *in-situ* and *ex-situ* clumps is based on their dark matter overdensity with respect to the host halo. We calculate the mean dark matter density within the clump radius of each off-center clump and the mean background dark matter density in the host halo at the clump position, averaged over a spherical shell about the disc center with a width equal to the clump diameter. When calculating the background density, all clumps were removed from the shell. The ratio of clump density to background density is denoted $1 + \delta_{\text{DM}}$, analogous to δ_ρ defined for the gas, §C. Figure 6 presents the probability density, $P(x)$, where $x \equiv \log(1 + \delta_{\text{DM}})$, for all off-center clumps. The distribution is clearly bi-modal, with a well defined peak at $x \gtrsim 0$ and a broader peak at $x \sim 2.5$. About 13% of the clumps contain no dark matter particles at all, placing them at $x = -\infty$, off the scale of Fig. 6. Based on this bimodality, we define *ex-situ* clumps as having $x > 1.5$. This happens to be similar to the selected threshold in $\log(\delta_\rho)$ between compact and diffuse gas clumps.

As a sanity check, we examined the stellar population of each *ex-situ* clump identified by its dark matter content. We find that in 94% of them, more than half the baryonic mass consists of stars formed outside the disc, as defined at the snapshot closest to the star

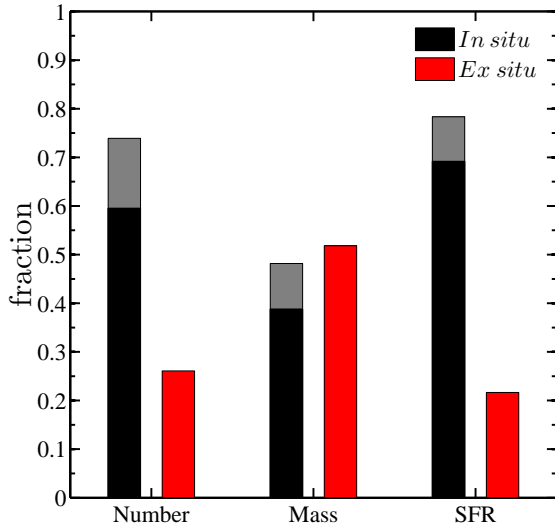


Figure 7. Census of *in-situ* vs *ex-situ* clump properties. Relative contribution of *in-situ* and *ex-situ* clumps to the off-center clump population in terms of number, baryonic mass and SFR. In the 3 *in-situ* bars, the black section signifies our conservative estimate, removing those clumps that are not co-rotating with their background or that have significant contributions to their masses from external stars. The grey sections at the top of the bars signify the contribution of these suspicious clumps. The *ex-situ* clumps are roughly 20 – 25% of the population in terms of number and SFR, though they contain $\gtrsim 50\%$ of the baryonic mass.

particle’s birth time. This is in agreement with what is expected of an external merger.

There is a small population of clumps in which more than half the baryonic mass consists of stars formed outside the disc while their dark-matter overdensity is low, which would have classified them as *in-situ* clumps. These constitute 8.5% of the clumps that have only little dark matter. We defer the analysis of the origin of these clumps to future work, but can raise here three possibilities. First, they could be *in-situ* clumps, which accreted an unusually large amount of disc stars that joined the disc earlier during mergers. Second, they could be *ex-situ* clumps that were stripped of their dark matter when they merged with the disc. Finally, they could be clumps formed by thermal or hydrodynamical instabilities in the cold streams feeding the disc.

3.2.3 Sharing the disc kinematics

We also study the degree of co-rotation of the off-center clumps with the rotation of the cold gas in their host disc. For each clump, we measured the center-of-mass velocity of its gas component in cylindrical coordinates in the disc frame, v_r, v_ϕ, v_z . These were compared to the mass weighted mean velocity and velocity dispersion of the cold gas in a cylindrical shell about the disc center at the clump position. The shell extends the thickness of the disc in the vertical direction and the diameter of the clump in the radial direction and all clumps were

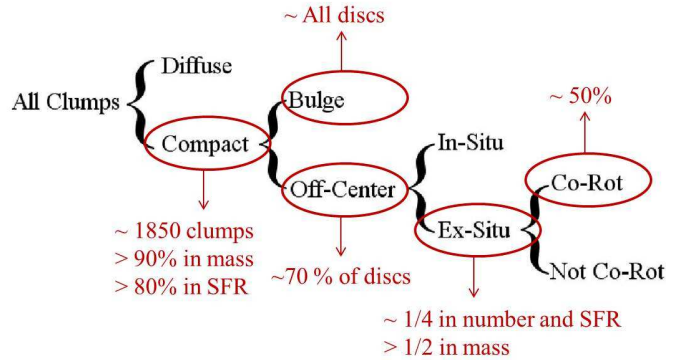


Figure 8. Schematic diagram of our clump classification scheme

removed from it. A clump is considered *co-rotating* with the disc if all three components of its velocity are within 2σ of the local mean disc rotation velocity.

We find that roughly half the *ex-situ* clumps are co-rotating with their host disc. Some of the properties of these co-rotating clumps are systematically different from the non-co-rotating ones, as will be discussed in §5. Among the clumps with low dark matter contrast that are classified *in-situ*, only 14% are not co-rotating with their host disc, exhibiting strong radial or vertical velocity components. Most of these are possibly *in-situ* clumps whose rotation pattern was severely perturbed due to dynamical interactions with other clumps or the surrounding disc. About 22% of those have large external stellar populations as well.

We have thus divided the off-center clumps into two major populations plus a minor intermediate population. First are the pure *in-situ* clumps, defined as clumps of low dark-matter contrast that are co-rotating with their background and have only small contributions to their mass from stars that formed outside the disc. Second are the pure *ex-situ* clumps, which have high dark matter content. Lastly, a small population of clumps with low dark-matter contrast but with either significant contributions from external stars or significant kinematic deviations from the local disc rotation. This intermediate population between *in-situ* and *ex-situ* clumps is sometimes referred to as *Is/Es*. However, since most of their properties are similar to those of the *in-situ* clumps (see §5), we commonly treat them as part of the *in-situ* class.

Figure 7 shows the fractions in number, baryonic mass and SFR of each population among all the off-center clumps. We can conservatively estimate that the *in-situ* clumps make up $\sim 60 - 75\%$ of the off-center population, contain $\sim 40 - 50\%$ of their mass and $\sim 70 - 80\%$ of their SFR, with the *ex-situ* clumps comprising the remainder. It is interesting to note that there is a significant contribution from *ex-situ* clumps, which make up at least a quarter of the off-center clump population and contribute more than half of the mass found in clumps. The intermediate population is minor, making up $\sim 15\%$ of all the off-center clumps and containing $\lesssim 10\%$ of their total mass and SFR.

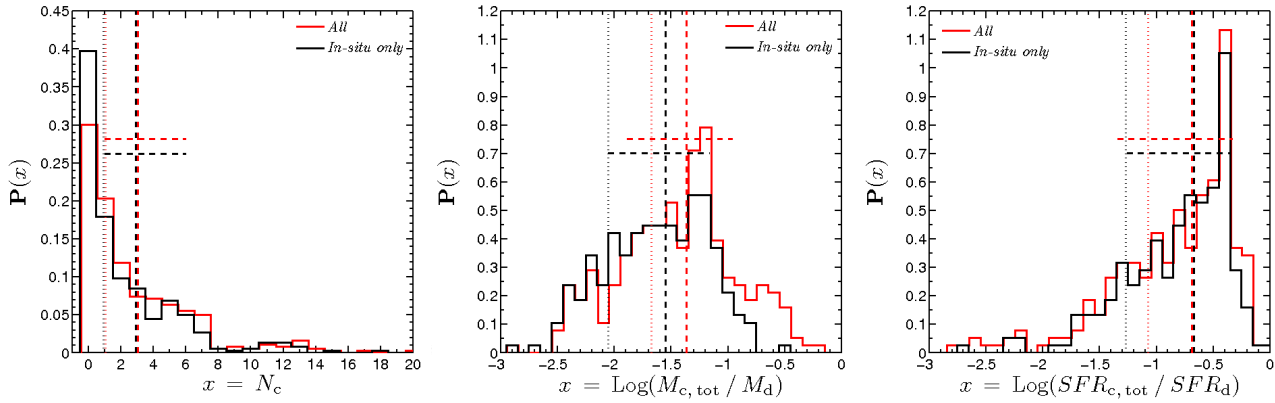


Figure 9. Clumpiness of our simulated discs. For the 380 discs in the redshift range $1.0 \leq z \leq 3.0$ having $\log(M_d) \geq 10.25$, we show the probability distributions of x : the number of clumps per disc (left), the log of the ratio of total baryonic mass in clumps to the disc baryonic mass (center) or the log of the ratio of total SFR in clumps to the disc SFR (right). The red histograms refer to all compact off-center clumps, while the black histograms refer only to *in-situ* clumps. Each histogram is normalized so that the integral over the entire disc population is equal to unity. However, in the center and right panels, those discs where $N_c = 0$, so that $x = -\infty$, are beyond the scale of the figure. Thus, the integral of the red histogram is roughly 0.7 and the integral of the black histogram is roughly 0.6, as can be read from the left panel. For “all” (*in-situ*) clumps, the vertical red (black) dotted lines mark the medians of the distributions including discs without any resolved clumps. The vertical red (black) dashed lines mark the medians considering only those discs where $N_c \geq 1$, while the corresponding horizontal lines encompass 67% of these discs about the median. The *ex-situ* clumps do not alter the distributions of the number of clumps per disc or the total SFR in clumps, but they can give rise to higher mass fractions.

3.2.4 Summary of clump classification

Figure 8 is a schematic diagram that summarizes our clump classification scheme. We begin by dividing all our clumps into *compact and round* versus *diffuse and elongated* based on their mean density residual and shape. The compact clumps contain $> 90\%$ of the mass and $> 80\%$ of the star formation of the clump population. Focusing on the *compact* clumps, we identify central *bulge* clumps versus *off-center* clumps. Nearly every galaxy hosts a compact *bulge* clump, while $\sim 70\%$ of the discs host *off-center* clumps. The *off-center* clumps are divided into *in-situ* and *ex-situ* clumps primarily based on their dark-matter density contrast with the host halo. The *ex-situ* clumps constitute roughly one quarter of the *off-center* clumps, but contain half the total mass. Finally, we find that the *ex-situ* clumps are divided roughly half and half into *co-rotating* and *non co-rotating* clumps.

All the numbers quoted above refer to clumps that are found in the extended disc. Restricting ourselves to the slim disc, we find that the number of *ex-situ* clumps is reduced by a factor of ~ 3 . This is to be expected, as the *ex-situ* clumps may spend time as satellites of the central disc, and may have large velocity components vertical to the disc. The number of *in-situ* clumps in the slim disc is smaller than in the extended disc by $\sim 30\%$. This is not surprising as many of the discs are warped away from the main disc plane (Fig. 2) such that clumps located in these extended arms may have formed there *in-situ*. We find that the distributions of properties of the clumps are similar in the extended disc and in the slim disc, so we restrict the remainder of our discussion to results pertaining to the extended disc. Besides giving us better clump statistics, these results are closer to

observations where the 2D images are integrated over more than the thickness of the gaseous disc.

4 DISC CLUMPINESS

In this section we study the distribution of discs in terms of their off-center clumpiness properties. Recall that the resolution of our simulations imposes an effective minimum clump mass of $\sim 10^{7.5} M_\odot$ in baryons. Indeed, we do not detect any compact clumps below this mass (Fig. 11). Since it appears clumps can have masses as low as $\sim 0.1\%$ of the mass of their host disc (Fig. 10), we conclude that in low mass discs with $M_d \lesssim 10^{10.5} M_\odot$, our sample of clumps must be incomplete. This effect is more severe at higher redshifts, since our galaxies are monotonically growing in time while the resolution scale remains fixed. In an attempt to minimize this effect, we limit our analysis in this section to the 380 discs in the redshift bin $1.0 \leq z \leq 3.0$ with masses $\log(M_d) \geq 10.25$. In these discs, our sample of gas clumps should be nearly complete down to $10^{-2.5} M_d$.

Figure 9 shows the probability density of (a) number of clumps per disc, (b) total baryonic mass in clumps relative to the disc baryonic mass (including the clumps), and (c) total SFR in clumps relative to the disc SFR (including the clumps). Separate histograms address the *in-situ* clumps alone and “all” the off-center clumps, *in-situ* plus *ex-situ*.

We read from the left panel of Fig. 9 that 70% of the discs host off-center clumps, and that 60% specifically host *in-situ* clumps. If we associate the appearance of at least one off-center *in-situ* clump with a VDI phase, we can conclude that the fraction of discs undergoing VDI at a given time is about 60%. If only clumps

more massive than 1% of the disc mass are considered, the fraction of clumpy discs becomes $\sim 55\%$ while the fraction of discs undergoing VDI becomes $\sim 42\%$. This represents a lower limit to the clumpy fraction of galaxies, which should be robust to the resolution, and is consistent with observed clumpy fractions (§7.2).

The average number of *in-situ* clumps per disc is ~ 2 , and the average number of “all” off-center clumps is ~ 3 , though the two distributions have a median value close to unity. Considering only the clumpy discs, the average (median) value of both distributions becomes ~ 4 (3). Recall, however, that the number of clumps may be subject to the threshold minimum clump mass imposed by the resolution. The shapes of the distributions are also rather similar, both gradually declining till $N_c \sim 8$ and then dropping sharply. In about 8% of the clumpy discs there are more than 8 clumps per disc, and in about 4% the number is larger than 12, with the record in our sample being 20 clumps per disc, 18 of them *in-situ*. This particular snapshot is visible in Fig. 1 and Fig. 2 at expansion factor $a = 0.34$, or $z \sim 2$. The *in-situ* clumps span a mass range of $10^8 - 10^9 M_\odot$ in baryons, while the disc mass is $\sim 3 \times 10^{10} M_\odot$.

The middle panel of Fig. 9 refers to the total baryonic mass in off-center clumps compared to the disc baryonic mass. This is more robust than the number of clumps because it is dominated by the more massive clumps and is therefore less sensitive to the minimum mass imposed by resolution. This figure shows that for discs undergoing VDI the median fraction of disc mass in *in-situ* clumps is $\sim 3\%$ ($\sim 1\%$ if all the discs are considered), though the probability density has a broad peak between 1% and 10%. Less than 3% of the discs have mass fractions larger than 15%. The value of the mass fraction addressed here is not straightforwardly constrained by Toomre instability theory. The fraction of mass in clumps compared to the cold mass in the disc, mostly gas and young stars, has been assumed in earlier works to be of order 20% based on a crude argument (DSC09) and on estimates from simulations (Ceverino et al. 2010; Elmegreen et al. 2007). Note that the current quote of a few to ten percent refers to the fraction of mass in clumps relative to the whole disc, which has a significant component of “hot” old stars. Crudely defining “hot” stars as being older than the time since the previous snapshot, roughly half an orbital time at the disc edge or 100 Myr, we find that they constitute on average $\lesssim 70\%$ of the disc baryonic mass. Taking this into account, the mass fraction of clumps with respect to the cold disk becomes 3-30%, consistent with the previous estimates.

Including *ex-situ* clumps as well, the median fraction of disc mass in “all” off-center clumps is 4% for the clumpy discs (and 2% for all the discs), with a peak near 6%. Indeed, *ex-situ* clumps tend to be more massive than the *in-situ* clumps. This is reflected in the tail of non-negligible probability to have a fraction 0.1 – 0.4 of the disc mass in clumps; about half *in-situ* and half *ex-situ* in the range 0.1 – 0.2 and all *ex-situ* above a fraction of 0.2.

The right panel of Fig. 9 addresses the fraction of

the SFR in off-center clumps compared to the whole disc. The distributions for *in-situ* clumps and “all” off-center clumps are similar, since most *ex-situ* clumps tend to have low SFR. For *in-situ* clumps in VDI discs the median SFR fraction is 22% (6% if all the discs are considered), and for “all” the off-center clumps in clumpy discs, the median is 20% (8% if all the discs are considered). Both distributions have similar modes, at $\sim 40\%$. In about 13% of discs undergoing VDI more than half the SFR is in clumps, and in about 3% the SFR fraction in clumps is more than 75%.

We attempted to address dependencies of the above statistics on disc mass and redshift, but detected mostly marginal or null trends. This is partly because of our limited sampling and partly because of the bias due to the fixed resolution scale in low mass disks and at high redshifts. The analysis is presented in an appendix §D. The most significant result is that the fraction of clumpy discs peaks for intermediate mass discs of $(1 - 3) \times 10^{10} M_\odot$ at all redshifts (Fig. D1). The fraction also seems to be higher at $z = 1 - 2$ than at $z = 2 - 4$. No systematic trend with either disc mass or redshift is apparent for the contribution of *in-situ* clumps to the total disc mass, suggesting that discs undergoing VDI turn a roughly constant fraction of their mass into clumps (see DSC09). *Ex-situ* merging clumps contribute more to the disc mass at higher redshift. This is consistent with the theoretical estimate that the timescale for mergers of a given mass ratio, in terms of the galaxy dynamical time, is shorter at higher redshift (Neistein & Dekel 2008).

5 DISTRIBUTIONS OF CLUMP PROPERTIES

We now turn to studying the properties of individual clumps and their distributions among the populations of clump types and within each population. The 1850 compact clumps in our sample are divided to 31% central *bulge* clumps, 51% off-center *in-situ* clumps (including 10% that are uncertain *Is/Es* clumps), and 18% off-center *ex-situ* clumps (half of which are co-rotating with the disc). Figure 10 shows the distributions of six clump properties for the different clump types. The probability densities for the *bulge* clumps, *in-situ* clumps and *ex-situ* clumps are together normalized to the total number of clumps. The quoted fractions of clump types allow a re-normalization of each histogram to a probability density normalized to unity for each clump type.

5.1 Mass

The top left panel of Fig. 10 refers to baryonic masses of individual clumps relative to their host disc, M_c/M_d .

In-situ clumps: For the *in-situ* clumps, the distribution of relative clump mass is close to lognormal, rather symmetric about a mean at $M_c/M_d = 0.01$, with a standard deviation of ~ 0.38 dex (FWHM ~ 0.7 dex). About 8% of the *in-situ* clumps are more massive than $0.03 M_d$, and less than 1% are more massive than $0.1 M_d$. The average of 0.01 is consistent with Toomre instability theory which predicts that the *in-situ* clumps

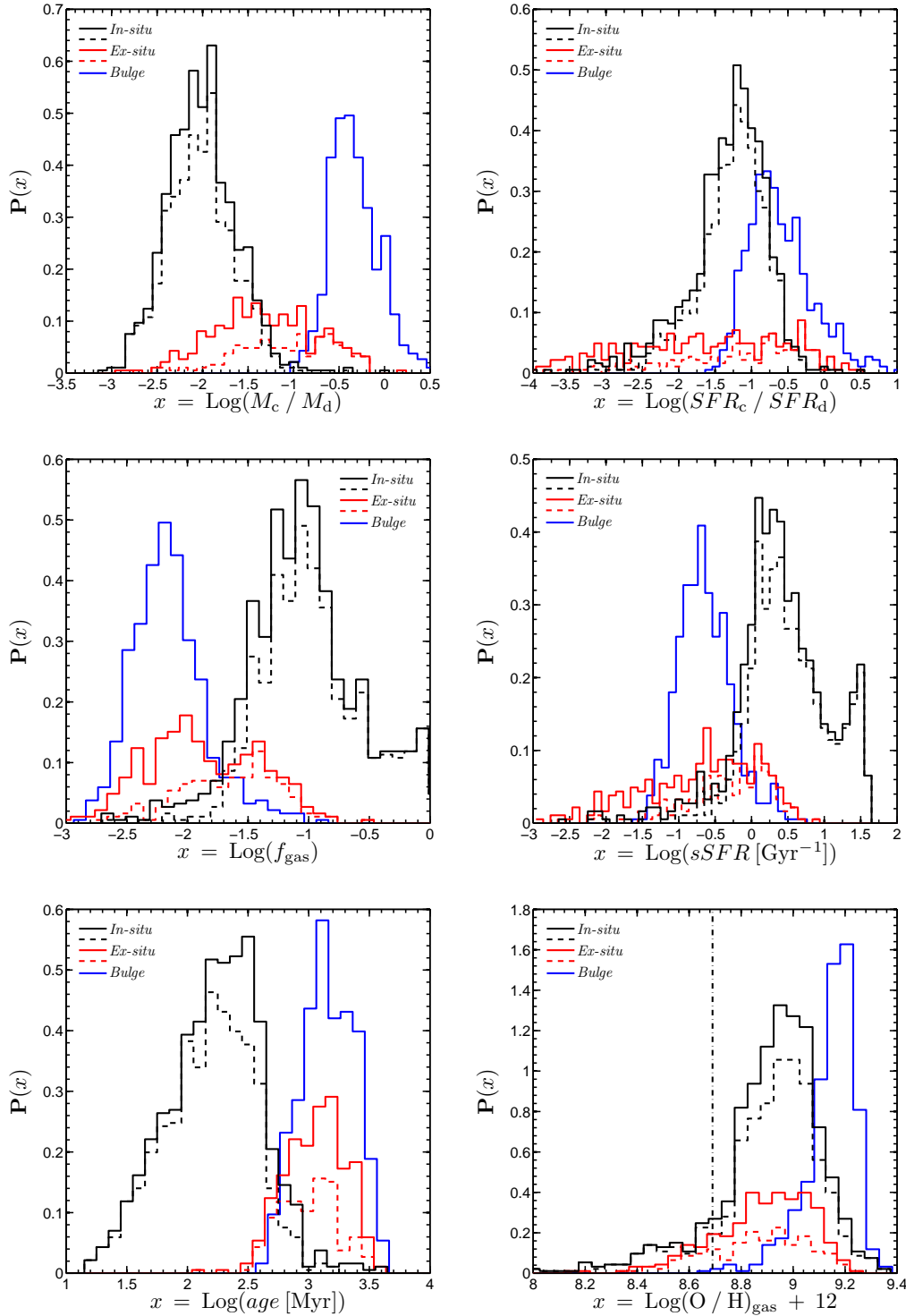


Figure 10. Clump properties. Each histogram is the probability density for the quantity defined as x . The three solid histograms refer to *bulge* clumps (blue), *in-situ* clumps (black) and *ex-situ* clumps (red). Also shown are the *in-situ* clumps without the uncertain cases (dashed black), and those *ex-situ* clumps that are co-rotating with the disc (dashed red). The distributions are normalized to the total number of compact clumps, such that the combined integrals under all three solid curves is equal to unity. Given that the *in-situ* clumps make up 51% of the population, the *bulge* clumps 31% and the *ex-situ* clumps 18%, each curve can be re-normalized to a probability density normalized to unity for each clump type. **Top row:** Clump mass relative to disc mass (left) and clump SFR relative to disc SFR (right). Disc properties were separated from bulge properties using the kinematic criterion defined in §2. **Middle row:** gas fraction (left) and sSFR (right). **Bottom row:** Mean stellar age (left) and gas metallicity (right, with solar metallicity marked by a dashed-dotted vertical line). *In-situ* clumps tend to be less massive, with younger stars and higher gas fraction and sSFR.

should each be a few percent of the cold mass in the disc (see DSC09 and references therein). We note that the least massive clumps are about $10^{-3}M_d$, higher than the minimum mass imposed by the resolution. The distribution of masses for the *Is/Es* clumps is similar to that of the whole *in-situ* population and they appear less massive than the *ex-situ* clumps, consistent with most of them being *in-situ* clumps.

Ex-situ clumps: The *ex-situ* clumps tend to be more massive than the *in-situ* clumps, with an average mass of $0.04M_d$. However, the scatter is large, roughly 1.5 dex FWHM, indicating that there is only a weak correlation between the mass of an *ex-situ* clump and that of its host disc, as expected from mergers. The co-rotating *ex-situ* clumps have systematically higher masses than the non-co-rotating ones. The average relative masses are 0.08 for the co-rotating clumps and 0.03 for the non-co-rotating ones. The possible origin of this phenomenon will be discussed in §7.

Bulge clumps: The central *bulge* clumps are rather massive. Since they may contain stars that do not kinematically belong to the disc, namely with $j_z / j_{max} < 0.7$ (§2), M_c/M_d can be larger than unity. The distribution of M_c/M_d for the *bulge* clumps is close to lognormal, with the mean at ~ 0.4 and a standard deviation of ~ 0.27 dex (FWHM = 0.7 dex). Recall that the mass of a *bulge* clump as defined here is a severe underestimate of the actual bulge mass (§3).

5.2 SFR

The top right panel of Fig. 10 refers to the SFR of individual clumps relative to their host disc, SFR_c/SFR_d .

In-situ clumps: For the *in-situ* clumps, the distribution of relative SFR is somewhat skewed; it has a narrower peak at high values and a tail extending to low values. In general, individual clumps contribute more to the disc SFR than to its mass. The mean SFR fraction is ~ 0.05 and the FWHM spread is ~ 0.9 dex. About 24% of the clumps contribute more than 10% of the disc SFR, and 2% contribute more than 30%. At the low end, about 13% of the *in-situ* clumps have SFRs smaller than 1% of the disc SFR. The low SFR tail is largely due to *in-situ* clumps older than 100 Myr located near or beyond R_d , mostly with below average gas fractions. Many of them are *Is/Es* clumps with external stellar populations, which tend to be among the oldest of the *in-situ* clumps, with ages of 300 – 800 Myr. Several of these have been tracked through time using their stellar particles and were found to have unusually large vertical motions and long migration times, thus exhausting their gas supply while still near the disc edge.

Ex-situ clumps: The distribution of relative SFR in *ex-situ* clumps appears to be even broader than the distribution of relative mass, and is nearly uniform in the range 0.001 – 1. The co-rotating *ex-situ* clumps have systematically higher SFRs than the non-co-rotating ones, in addition to higher masses. The average relative SFRs are 0.12 and 0.004 for the

co-rotating and non-co-rotating clumps respectively. Possible implications of this will be discussed in §7.

Bulge clumps: The SFR in the *bulge* clumps tends to be higher than in the off-center clumps, with the average of SFR_c/SFR_d at 0.23 and a FWHM of 0.8 dex. In about 10% of the cases the SFR in the central *bulge* clump is higher than the disc total. Such high SFRs characterize the *bulge* clumps as compact “blue nuggets”, resulting from intense gas inflow into the disc center (Cheung et al. 2012; Barro et al. 2013; Dekel & Burkert 2014).

5.3 Star-Formation in Clumps I: Gas Fraction

The second and third rows of Fig. 10 present distributions of properties relating to star-formation within the clumps: gas fraction, sSFR, stellar age and metallicity. We do not attempt to produce reliable colors prior to implementing dust and radiative transfer. However, ignoring dust reddening, blue colors should be associated with high gas fractions, high sSFRs, young ages and low metallicities.

The left-center panel in Fig. 10 refers to the gas fractions with respect to the baryonic mass within the clumps. While the overall gas fractions at $z \sim 2$ are underestimated in the current simulations (§2), the relative values and distributions for the different clump types are likely to be more reliable.

In-situ clumps The *in-situ* clumps are fairly gas rich, far more so than the other clump types, as expected from their formation by instability in gas-rich discs. The median of the distribution of gas fraction is at roughly 0.08, with the peak at $\sim 0.09 - 0.1$ and a FWHM of ~ 0.8 dex. There is a tail extending to low gas fractions, as well as a significant population of very gas rich clumps. Roughly 14% of the clumps have gas fractions below 0.03 and 3% have fractions below 0.01. This gas-poor tail is mostly due to *Is/Es* clumps with old stellar ages, corresponding to the low SFR tail discussed above. At the gas-rich end, 12.5% of the clumps have gas fractions above 0.3, 8% have values above 0.50 and 3.5% have gas fractions above 0.75. These very gas rich clumps have very low stellar masses (though not unusually large gas masses) and young stellar ages, with high sSFR and low metallicity. They are located near the edge of the disc and appear to be newly formed clumps undergoing an initial burst of star-formation.

Ex-situ clumps The *ex-situ* clumps have on average much lower gas fractions than the *in-situ* clumps, with a median value of about 0.01. However, the co-rotating clumps have systematically higher gas fractions than the non-co-rotating ones, giving rise to an almost bi-modal distribution. The co-rotating clumps have an average gas fraction of roughly 0.02, with the peak of their distribution at 0.04 and 10% of them having gas fractions above 0.06. On the other hand, the average gas fraction of non-co-rotating *ex-situ* clumps is ~ 0.007 , with the peak roughly at 0.01. Only 4% of them have gas fractions greater than 0.06, while over 15% have values below 0.003, compared to only 3% of the co-rotating clumps. This may indicate late gas

accretion onto co-rotating *ex-situ* clumps, as discussed further in §7.

Bulge clumps The *bulge* clumps have a similar distribution to the non-co-rotating *ex-situ* clumps. The average gas fraction is 0.006 and the FWHM = 0.6 dex. There is a tail towards higher values, with roughly 3% of the clumps having gas fractions above 0.03. These correspond to young bulges at redshifts $z > 3$.

5.4 Star-Formation in Clumps II: sSFR

The right-center panel in Fig. 10 refers to the sSFR in the clumps, defined as SFR divided by stellar mass. Given our crude estimate for SFR, this amounts to $(M_{*,c}(< \Delta t)/\Delta t)/M_{*,c}$, where $\Delta t = 30$ Myr and $M_{*,c}(< \Delta t)$ is the mass in stars younger than Δt within the clump. This has a maximum possible value of $1/\Delta t = 33.33 \text{ Gyr}^{-1}$, attained when $M_{*,c}(< \Delta t) = M_{*,c}$, or in other words when all of the stars in the clump are younger than 30 Myr.

In-situ clumps The *in-situ* clumps have very high sSFRs, with a median value of $\sim 2.1 \text{ Gyr}^{-1}$ ($\sim 2.5 \text{ Gyr}^{-1}$ without the *Is/Es* clumps), a natural result of their high gas fractions. The distribution peaks at around 1.7 Gyr^{-1} and has a FWHM spread of ~ 0.9 dex. With such high sSFRs and gas fractions, the *in-situ* clumps should appear quite blue in observations, provided that there is no significant dust reddening.

There is, however, a tail towards low sSFR, with 4% of the clumps having values below 0.1 Gyr^{-1} . These clumps also occupy the tail of low gas fractions discussed above, and are dominated by *Is/Es* clumps whose stellar ages are over 300 Myr near the outskirts of the disc. Note that there are also many *Is/Es* clumps with high sSFRs of 2 Gyr^{-1} or more, similar to the bulk of the *in-situ* population and higher than the typical values for *ex-situ* clumps.

Also interesting is the prominence of a second peak in the distribution, at around $\sim 30 \text{ Gyr}^{-1}$. The peak itself and its sharp break at higher values is a numerical artifact, due to our crude estimate of SFR, which does not resolve star-formation on timescales shorter than 30 Myr. This causes all the clumps which might have had sSFRs above 30 Gyr^{-1} to pile up around this value, even though the intrinsic distribution is more likely an extended tail to very high sSFR values. A robust statistic is that roughly 16% of the *in-situ* clumps have sSFRs higher than 10 Gyr^{-1} . These extremely efficient star-forming clumps coincide with the very gas rich clumps discussed above, with an average gas fraction of 0.46. They have very young ages of 65 Myr on average. Their stellar masses are low, with an average of $8 \times 10^7 M_{\odot}$. Their metallicities are sub solar, averaging to $(\log((O/H)+12) \simeq 8.63$ and 8.40 for the gas and stars, respectively. Finally, they tend to be located near the edge of the disc. In other words, these are newly formed clumps undergoing their first burst of star formation.

Ex-situ clumps The *ex-situ* clumps have much lower sSFR than the *in-situ* clumps, similar to their relative gas fractions. We thus expect *ex-situ* clumps to appear redder in observations. The median sSFR

is 0.2 Gyr^{-1} , but the distribution is very broad and skewed towards low values. About 12% of the *ex-situ* clumps have sSFR below 0.01 Gyr^{-1} while 6% have values above 2 Gyr^{-1} . As expected from their bi-modality in gas-fraction, the co-rotating *ex-situ* clumps have significantly higher sSFR values than the non-co-rotating ones, with median values of 0.5 and 0.06 Gyr^{-1} respectively.

Bulge clumps The *bulge* clumps have a median sSFR of 0.2 Gyr^{-1} and a fairly symmetric distribution about this value, with a standard deviation of 0.37 dex (FWHM = 0.7 dex). There is a tail towards high sSFR, with 4.5% of the clumps having values above 1 Gyr^{-1} , corresponding to those with high gas fractions.

5.5 Star-Formation in Clumps III: Stellar Age

The bottom left panel of Fig. 10 refers to the mass-weighted mean stellar age of the clumps, calculated with all the stars present in the clump.

In-situ clumps The *in-situ* clumps are fairly young, with a median age of ~ 160 Myr and a broad peak from $\sim 150 - 300$ Myr, on the order of 1-2 orbital times at the edges of the discs, which is the expected migration time of clumps to the disc center (DSC09; Ceverino et al. 2010, 2012). The FWHM of the distribution is 0.65 dex, but it is skewed towards younger ages. 30% of the clumps are younger than 100 Myr and 13% are younger than 50 Myr. On the other hand, only 20% of the clumps are older than 300 Myr and 7% are older than 500 Myr, most of them *Is/Es* clumps, where more than 50% of the mass is in stars formed outside the disc. *In-situ* clumps are not expected to survive for much longer than a couple of orbital times, which explains the sharp drop of the distribution towards older ages. We note here that a model where clumps disrupt shortly after they form due to intense feedback would predict much younger ages for clumps, of order $\lesssim 50$ Myr, with a much smaller age spread (see discussion in §7.1).

We find the *in-situ* clumps to be, on average, older at lower redshift. At $4.0 < z < 2.5$, their average age is ~ 100 Myr, as opposed to ~ 200 Myr at $1.0 < z < 1.5$. The standard error of the mean in these two redshift bins is only 0.04 dex and 0.02 dex, respectively, so the difference appears significant. This is interpreted as an increase in the disc orbital time at lower redshifts, due to the cosmological density decrease, and a corresponding increase in the clump migration time.

Ex-situ clumps The *ex-situ* clumps are much older than the *in-situ* clumps. Their median age is ~ 1.1 Gyr, while their distribution peaks at 1.6 Gyr with a FWHM spread of 0.7 dex. The distribution is very similar to that of the *bulge* clumps, unsurprising, as the *ex-situ* clumps are largely bulges of little merging galaxies. We also note an increase in the average age of *ex-situ* clumps from high to low redshifts. At $4.0 < z < 2.5$ the average age is ~ 620 Myr while at $1.0 < z < 1.5$ it is ~ 2200 Myr, with a standard error of the mean of less than 0.02 dex. This variation was expected, since

the *ex-situ* clumps are simply external, merging galaxies which age along with the Universe. At all redshifts, the *ex-situ* clumps have systematically lower gas fractions and sSFRs and much older ages than the *in-situ* clumps, and will likely appear systematically redder.

Bulge clumps Unsurprisingly, the *bulge* clumps contain old stellar populations with median ages of ~ 1.3 Gyr (FWHM = 0.5 dex). At all redshifts, *ex-situ* and *bulge* clumps have very similar age distributions.

5.6 Star-Formation in Clumps IV: Metallicity

The bottom right panel of Fig. 10 refers to gas-phase metallicity in units of $\log(O/H) + 12$. Solar metallicity in these units is 8.69 (Asplund et al. 2009). Note that the same effect which causes an underestimate of gas fractions in the current simulations may also cause elevated metallicity values in our galaxies, but we can still trust the relative values of the different clump types.

In-situ clumps The metallicity in the *in-situ* clumps is high, and nearly all clumps have super solar metallicity in both gas and stars. They have a median gas-phase metallicity of $\log(O/H) + 12 \sim 8.9$, with a FWHM spread of 0.35 dex. There is also a tail extending to sub-solar values, containing 13% of the clumps, and dominated by the young, gas-rich, star-forming clumps discussed above.

Ex-situ clumps The distribution of gas-phase metallicity for the *ex-situ* clumps closely resembles that of the *in-situ* clumps in the median, peak and width of the distribution. The *ex-situ* clumps also exhibit a similar tail to sub-solar values, dominated by the co-rotating clumps. This result suggests that most of the gas found in those *ex-situ* clumps which have gas, i.e. the co-rotating ones, was accreted from the disc and is the same gas that formed the *in-situ* clumps.

Bulge clumps The *bulge* clumps have the highest metallicity values, with a median value of 9.1 and a narrow FWHM of 0.3 dex. Less than 1% of the clumps have sub-solar metallicity.

6 GRADIENTS OF CLUMP PROPERTIES

Here we investigate the properties of the off-center clumps as a function of distance from the disc center, and especially search for systematic radial variations that characterize the *in-situ* and the *ex-situ* clumps in comparison with the corresponding gradients in the background disc. The theoretical implications of such variations for distinguishing between clump migration versus rapid disruption are discussed in §7.1. In the profiles shown in Fig. 11 and Fig. 12, the radial distance d is measured in terms of the disc radius R_d . Points represent the *in-situ* clumps (grey circles and green diamonds) and *ex-situ* clumps (red squares). The corresponding medians and 67% scatter within bins of d/R_d are marked. The medians for all off-center clumps (large magenta circles) follow the values for *in-situ* clumps within the disc radius. Significant contamination from *ex-situ* clumps is visible only at

$d \geq R_d$. The radial profiles in the inter-clump disc are shown for comparison (dashed blue).

6.1 Mass

The top left panel of Fig. 11 refers to the baryonic mass of clumps and the top right panel refers to the profile of stellar surface density within the clumps.

In-situ clumps The *in-situ* clumps show a strong gradient in mass, with the median values exhibiting a logarithmic slope of -0.60 ± 0.06 . The profile is better fit by a broken power law, with a slope of -0.85 ± 0.07 exterior to $0.3R_d$ and a slope of -0.40 ± 0.08 interior to this radius. The median mass increases from $2-3 \times 10^8 M_\odot$ near R_d to $\sim 8 \times 10^8 M_\odot$ near $0.1R_d$. This is consistent with the clumps preferentially forming at large radii and accreting mass from the disc as they migrate inward (§7.1). Alternatively, clumps may also form at small radii and be more massive there to begin with, possibly due to the larger fraction of cold mass at small radii. However, the gradient in clump ages (Fig. 12) argues against this, as there are almost no clumps younger than 100 Myr interior to $0.4R_d$.

Nearly all the *in-situ* clumps have stellar surface densities higher than the local background disc by an order of magnitude or more. This is reassuring, since our clumps were identified in gas and it was not clear a priori that they would contrast strongly with the stellar background in the disc and could be associated with observed stellar clumps. The exceptions, with stellar surface densities only a few times greater than the background, are all found at large radii and correspond to young, gas rich clumps with high sSFR. These clumps may not be observable in stellar maps of the galaxy, but may be detectable in H α . The best-fit power law to the profile of median values in the range $0.1 < d/R_d < 1$ yields a slope of -0.65 ± 0.13 , shallower than the corresponding slope of -1.88 ± 0.1 in the background disc. The median clump surface density increases from $\Sigma_* \sim 10^3 M_\odot \text{pc}^{-2}$ at R_d to $\Sigma_* \sim 10^4 M_\odot \text{pc}^{-2}$ near $0.1R_d$.

Ex-situ clumps The *ex-situ* clumps tend to be more massive than the *in-situ* clumps at every radius, by a factor of 3-4 in the median. The median profiles appear to have similar slopes. This may indicate that *ex-situ* clumps, especially the co-rotating ones, also migrate inward and accrete mass from the disc. However, the scatter of masses for the *ex-situ* clumps is larger, as massive *ex-situ* clumps are naturally present at all radii. Similarly, the median surface densities of the *ex-situ* clumps are a factor 3-4 higher than those of the *in-situ* clumps at all radii. At large radii one can find *ex-situ* clumps with surface densities three orders of magnitude above the background. This would be a clear signal for an *ex-situ* clump, as *in-situ* clumps are not expected to exhibit such high stellar surface densities, especially near the disc edge. Closer to the center, the difference between the *in-situ* and *ex-situ* clumps becomes less pronounced, as the *in-situ* clumps have formed many more stars during their migration.

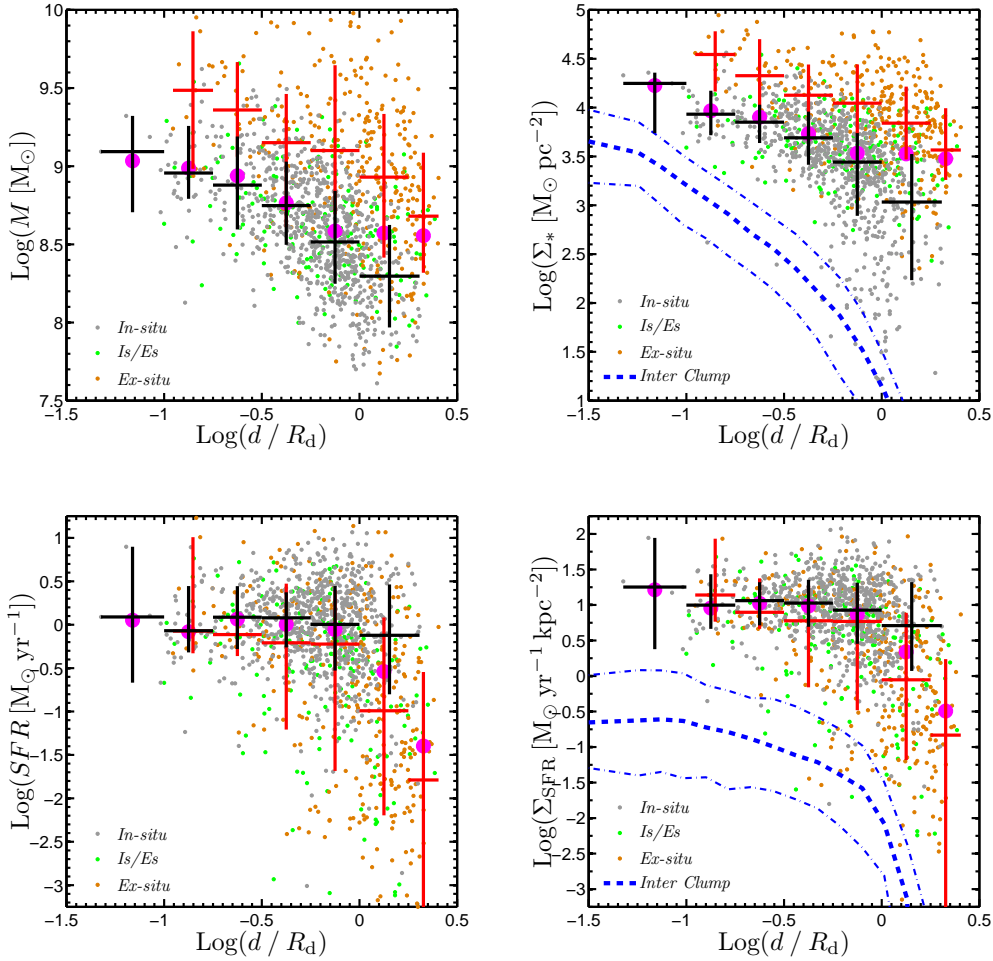


Figure 11. Gradients of various properties across the disc. The x axes are all $\log(d/R_d)$, where d is the galactocentric distance and R_d is the radius of the host disc. The grey points are the values for the *in-situ* clumps without the suspicious *Is/Es* cases, which are marked in green. The orange points are for the *ex-situ* clumps. The black crosses show the median values for the *in-situ* clumps in 6 equally spaced bins of $\log(d/R_d)$. The horizontal bar spans the width of the bin while the vertical bar marks the 67% scatter about the median. The red crosses show the same, but for the *ex-situ* clumps. Large magenta circles show the median values for all off-center clumps. The thick blue dashed lines in the two right-hand panels show the median profiles for the inter-clump medium in all our clumpy discs (the discs hosting the plotted clumps). These values were calculated in rings extending the thickness of the disc in the vertical direction with all clumps removed from them. The thin dot-dashed blue lines mark the 67% scatter about the median. **Top row:** Baryonic mass (left) and stellar surface density (right). **Bottom row:** SFR (left) and SFR surface density (right). Note that the masses and SFRs are absolute values, not normalized to the disc total. The clump surface densities were calculated in a face on projection of the disc, using their projected surface areas. The *in-situ* clumps are more massive nearer the disc center though their SFR values have no systematic radial variation.

6.2 SFR

The bottom left panel of Fig. 11 refers to the SFR in clumps and the bottom right panel refers to the profile of star-formation rate surface density. The sharp drop in the disc Σ_{SFR} near R_d corresponds to the edge of the gas disc as defined using the density profile of cold gas, beyond which stars simply cannot form.

In-situ clumps The *in-situ* clumps do not show a systematic radial variation of the SFR, with the median values quite constant at $1 - 2 M_\odot \text{yr}^{-1}$. This seems to require a replenishment of gas supply during migration inward, again hinting at accretion of fresh gas from the disc into the clumps. The *in-situ* clumps also exhibit a fairly constant SFR surface density, $\Sigma_{SFR} \sim$

$10 - 20 M_\odot \text{yr}^{-1} \text{kpc}^{-2}$. This is a factor of $\sim 50 - 100$ above the local background, making the clumps appear as distinct peaks of enhanced SFR. The outliers with low Σ_* discussed above have particularly high Σ_{SFR} values. In both mass and SFR, the *Is/Es* clumps are indistinguishable from the *in-situ* clumps.

Ex-situ clumps The *ex-situ* clumps tend to have lower SFRs, and especially so near or outside R_d , where the median SFR drops to below $0.1 M_\odot \text{yr}^{-1}$. Interior to R_d , the median SFR in the *ex-situ* clumps is on the order of $0.5 M_\odot \text{yr}^{-1}$, albeit the scatter is much larger than for the *in-situ* clumps. Their Σ_{SFR} exhibits a similar behaviour. At all radii interior to R_d , the *ex-situ* clumps have values a factor of ~ 2 below the *in-situ*

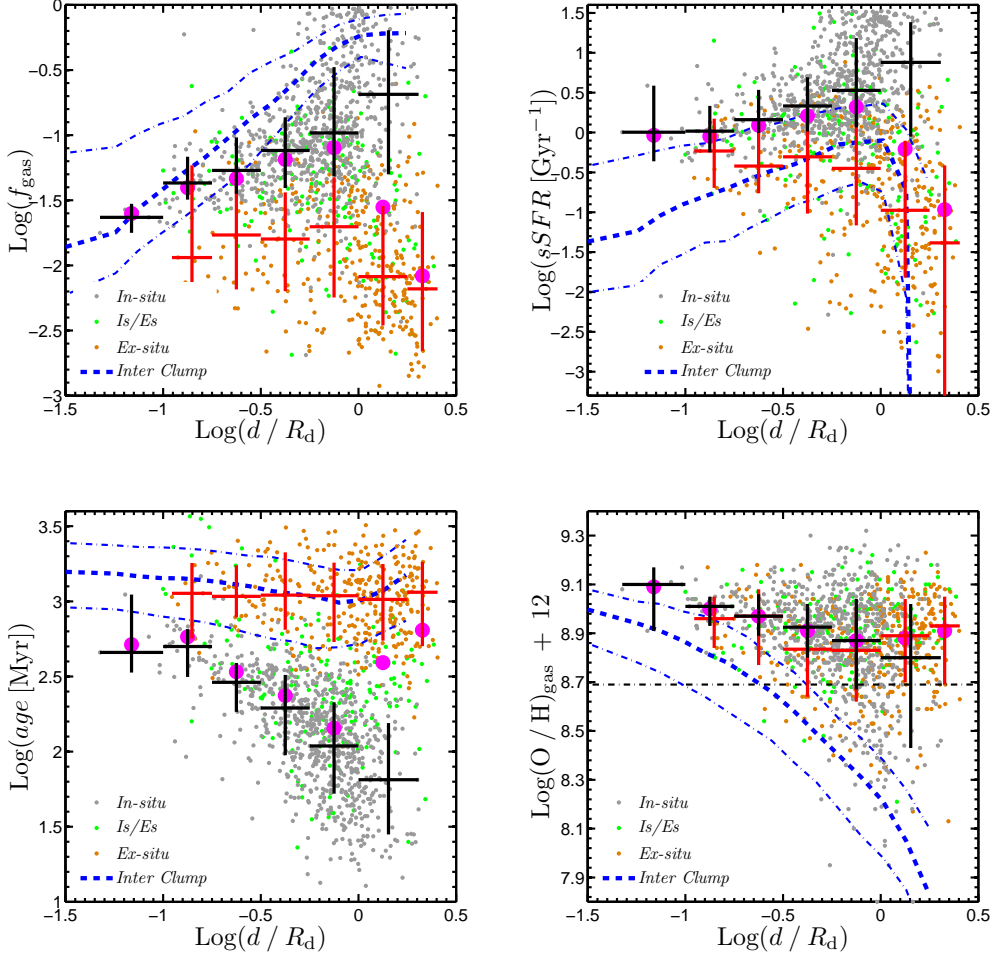


Figure 12. Same as Fig. 11, gradients of clump properties across the disc. **Top row:** Gas fraction (left) and sSFR (right). **Bottom row:** Stellar age (left) and gas metallicity (right, with solar metallicity marked). The *in-situ* clumps are older, with lower specific SFRs, lower gas fractions and higher metallicities nearer the disc center and the gradient is steeper than the underlying smooth component. Near the disc edge, the *ex-situ* clumps have older stellar ages, lower gas fractions and lower sSFR values.

clumps, but still more than an order of magnitude above the background.

6.3 Gas Fraction, sSFR and Age

The top two panels of Fig. 12 refer to the gas fraction (left) and sSFR (right), while the bottom left panel refers to the stellar age. These three properties trace the star-formation within the clumps and best distinguish the *in-situ* from the *ex-situ* clumps.

In-situ clumps Between $0.1R_d$ and R_d , the *in-situ* clumps' median gas fraction has a logarithmic slope of $+0.52 \pm 0.04$. Including clumps at larger and smaller radii gives a slope of 0.67 ± 0.05 . This is shallower than the underlying gradient in the inter-clump background, which has a slope of 1.24 ± 0.02 . Near $0.1R_d$, the median gas fraction in *in-situ* clumps is roughly 3%, comparable to the background (but recall that the absolute values in the current simulations at $z \sim 2$ are underestimates, §2). Near R_d , however, the median gas fraction in *in-situ* clumps is about 10-20%, roughly a factor of 3 below the

background. Many clumps near R_d are almost totally gaseous, and thus undetectable in stellar maps; these are the clumps with very low Σ_* , which make up the high end of the gas fraction distribution in Fig. 10. On the other hand, we note that the gas mass of the *in-situ* clumps (not shown) does not exhibit a clear trend with distance. The above is consistent with a preferred formation of *in-situ* clumps at large radii, followed by accretion of gas from the disc onto the clumps such that the decreasing gas fractions at smaller distances result from increasing stellar masses due to star formation.

The *in-situ* clumps constitute peaks in the sSFR distribution, with median values a factor of ~ 5 above the disc at all radii. In the range $0.1R_d < d < R_d$, the logarithmic slope of the median sSFR in *in-situ* clumps is $+0.68 \pm 0.04$, though this steepens to $+0.82 \pm 0.09$ including clumps at $d \geq R_d$. For the inter-clump material the slope is $+0.84 \pm 0.03$. Near R_d the *in-situ* clumps exhibit a median sSFR of $\sim 5 \text{ Gyr}^{-1}$, though many clumps have values above 10 Gyr^{-1} , as we saw in Fig. 10. These are newly formed clumps with very high

gas fractions and young ages. Near $0.1R_d$, the median value drops to 1 Gyr^{-1} .

The age gradient of the *in-situ* clumps is rather steep. The median age exterior to $0.1R_d$ has a logarithmic slope of -0.86 ± 0.03 , rising from $\sim 80 \text{ Myr}$ near R_d to $\sim 500 \text{ Myr}$ near $0.1R_d$. This is consistent with the clumps starting to form stars in the outer disc and then gradually migrating inwards. The age gradient in the smooth inter-clump component is much shallower, with a slope of -0.20 ± 0.01 in the same range. This suggests a separate evolution of the clumps and the smooth component.

Ex-situ clumps The *ex-situ* clumps show no clear radial gradient in any of the properties related to star formation, except for a tendency of clumps interior to R_d to have higher gas fractions and sSFRs than those outside R_d . Interior to R_d , the *ex-situ* clumps exhibit median gas fractions of 1-2%, sSFRs of $\sim 0.4 \text{ Gyr}^{-1}$ and ages of $\gtrsim 1 \text{ Gyr}$, roughly independent of distance. Beyond R_d , the gas fractions and sSFR drop sharply while the age remains constant. The profiles of age and sSFR in the *ex-situ* clumps appear very similar to those of the background disc at all radii.

Since the *in-situ* clumps dominate the off-center clump population within R_d , the gradients in this region do not change dramatically even if the *in-situ* and *ex-situ* populations are mixed together. The gradients of the median values for clump gas fraction, sSFR and stellar age including all the off-center clumps in the range $0.1R_d < d < R_d$ are, respectively, 0.43 ± 0.04 , 0.49 ± 0.02 and -0.79 ± 0.05 , only slightly shallower than the values quoted above for the *in-situ* clumps only. The signal should therefore still be detectable observationally, provided the clumps are properly resolved from the inter-clump disc component. At large distances $d \geq R_d$, however, significant contamination from *ex-situ* clumps is evident, which causes a distinct break in the profile.

The difference between the properties associated with gas and star formation of the *in-situ* and *ex-situ* clumps can provide an observable distinction between them. We see that massive clumps near the disc edge that have old ages, low sSFR and low gas fractions, namely are red in color, are almost exclusively *ex-situ* clumps. *In-situ* clumps at these large radii are dominated by young stars and have high sSFR and gas fractions, namely they should be blue unless reddened by dust. These differences are less pronounced at smaller radii, as the stars in the *in-situ* clumps have partly aged and their sSFR and gas fractions have decreased, while the *ex-situ* clumps have not evolved noticeably.

The population of *Is/Es* clumps have values in between the values for the two main populations. However, they exhibit a large scatter and there is no significant gradient. This population could thus weaken the observable gradients of the *in-situ* clumps, but this is hopefully a small effect.

6.4 Metallicity

The bottom right panel of Fig. 12 refers to the gas metallicity. As we saw in Fig. 10, the *in-situ* and the *ex-situ* clumps have fairly similar distributions. However, while the *ex-situ* clumps show no clear gradient with distance, the *in-situ* clumps systematically become more metal rich as they near the center, as expected from clump migration. Their median value increases from $\log(O/H) + 12 \sim 8.8$ near R_d to a value of $\gtrsim 9$ near $0.1R_d$, with a logarithmic slope of -0.20 ± 0.01 . This gradient is much shallower than in the inter-clump gas. While the metallicity is similar for the clumps and the disc near the center, at large radii the clumps appear much more metal rich than the background, suggesting self enrichment of the clumps independently from the disc. Note that the lower envelope of clump metallicity, both for *in-situ* and *ex-situ* clumps, closely follows the background disc median, consistent with accretion of fresh gas from the disc onto the clumps which they then use to form new stars. The large tail of sub-solar metallicity clumps visible in Fig. 10 exists only at large radii, and corresponds to the very young, very gas rich and highly star forming clumps.

7 DISCUSSION

7.1 Clump Survival versus Disruption

One could compare two extreme scenarios concerning the life and fate of high-redshift giant clumps formed by VDI. In one scenario (I), as in our current simulations, the clumps, despite undergoing outflows, remain intact and even grow by accretion as they migrate into the disc center on an orbital timescale, $\sim 250 \text{ Myr}$ at $z \sim 2$. In the competing scenario (II), the clumps disrupt on a dynamical timescale, $\sim 50 \text{ Myr}$ at $z \sim 2$, well before they complete their migration.

On the theory side, DSC09, based on Dekel & Silk (1986), estimated that supernova feedback may not have enough power to disrupt the clumps on a dynamical timescale. Murray et al. (2010) argued that momentum-driven radiative stellar feedback could disrupt the clumps on a dynamical timescale, as it does in the local giant molecular clouds. Then Krumholz & Dekel (2010) showed that such an explosive disruption is not expected to occur in the high-redshift giant clumps unless the SFR efficiency in a free-fall time is $\epsilon_{\text{ff}} \sim 0.1$, much larger than what is implied by the Kennicutt relation at $z = 0$. Such a deviation from the local Kennicutt law is inconsistent with observations (Tacconi et al. 2010, 2013; Freundlich et al. 2013).

Dekel & Krumholz (2013) proposed instead that the observed outflows from high-redshift clumps (Genzel et al. 2011; Newman et al. 2012), with mass loading factors of order unity, are driven by steady momentum-driven outflows from stars over many tens of free-fall times. Their analysis was based on the finding from simulations that radiation trapping is negligible because it destabilizes the wind

(Krumholz & Thompson 2012, 2013). Each photon can therefore contribute to the wind momentum only once, so the radiative force is limited to $\sim L/c$. When combining radiation, protostellar and main-sequence winds, and supernovae, Dekel & Krumholz (2013) estimated the total direct injection rate of momentum into the outflow to be $\sim 2.5L/c$. The adiabatic phase of supernovae and main-sequence winds can double this rate. They conclude that most clumps are expected to complete their migration prior to gas depletion. Furthermore, as described below, the clumps are expected to double their mass in a disc orbital time by accretion from the disc and clump-clump mergers, so their mass actually grows in time and with decreasing radius within the disc.

Given the uncertainties in the theoretical analysis, it is worthwhile to consider, simulate and compare different scenarios where the feedback strength is pushed to extreme limits, such as scenarios I and II. Genel et al. (2012b) simulated scenario II by implementing in their SPH simulations a phenomenological, “sub-grid”, model for producing extreme galactic super-winds, and indeed got the clumps disrupted. Hopkins et al. (2012) obtained similar results in isolated disc SPH simulations which implemented both short and long range radiative feedback. Trapping factors were calculated using the optical depth from the center of the clump to the surface, which is likely to overestimate the realistic effect of radiative feedback by a an order of magnitude (Krumholz & Thompson 2012, 2013; Dekel & Krumholz 2013). Detailed statistics of clump properties in scenario II are yet to be performed. The clump properties in our current simulations of scenario I, especially their gradients and relation to the off-clump gradients in the disc as discussed in §6, can help us come up with observables that will distinguish between the two extreme scenarios.

The accretion of material from the disc onto the clumps during their migration is another distinct prediction of scenario I. Ignoring outflows from clumps, we can crudely estimate this accretion rate as follows. A collapsed clump accretes material from its tidal radius, which in a $Q \sim 1$ disc is roughly its Toomre radius, R_T . This is the initial size of the proto-clump patch prior to collapse, where self gravity overcomes pressure and rotation support. Assuming that the surface density in the proto-clump was roughly equal to the mean surface density in the disc, the initial clump mass is $M_c = M_d(R_T/R_d)^2$, where M_d and R_d are the disc mass and radius. We parameterize the background density at the clump position as a factor α times the mean density in the disc: $\rho = \alpha M_d/(2\pi R_d^2 H_d)$. If the disc is exponential with a constant scale height, and R_d is roughly twice the effective radius (which contains 85% of the mass) then $\alpha \sim 0.23$ at the disc edge and 1.23 at $0.5R_d$. During its migration, the relative velocity between the clump and the surrounding medium is roughly σ , the velocity dispersion in the disc, which is assumed to be isotropic and the same for all the cold disc components. Vertical stability in the disc thus tells us that $\sigma/V_d \sim H_d/R_d$, where V_d is the

rotation velocity in the disc. The clump accretion rate thus becomes $\dot{M}_c = \pi R_T^2 \rho \sigma = M_c(\alpha/2)(V_d/R_d)$, so the accretion time is $t_{acc} \equiv M_c/\dot{M}_c = 2\alpha^{-1}t_d$, where $t_d = R_d/V_d$ is the crossing time. Following section 4 of DSC09 we approximate the clump migration time as $t_{mig} \sim 8t_d$, so the relative increase in clump mass during migration is $\Delta M_c/M_c \sim 4\alpha$, which is roughly 2 if the effective α for the clump during its migration is roughly 0.5. Thus, the clump can triple its mass during migration from accretion alone. This is consistent with the mass gradient for clumps in Fig. 11. A steady accretion of fresh gas onto the clumps during their migration may also explain the lack of radial trend in their average SFR, as the gas supply is constantly replenished. The fact that the *ex-situ* clumps show a similar mass gradient, may suggest that at least the co-rotating ones accrete mass in a similar fashion.

The other gradients can be understood in the following way. We assume that the *in-situ* clumps form from patches within the disc having initial gas fractions and stellar distributions similar to the local background where they formed. However, as the SFR in clumps is more intense than in the inter-clump medium (van den Bergh 1996; Elmegreen et al. 2004b; Elmegreen & Elmegreen 2005; Förster Schreiber et al. 2006; Genzel et al. 2008; Guo et al. 2012; Wuyts et al. 2012), they quickly become dominated by a young stellar population, which outweigh and outshine the older stars that the clump inherited from the disc. During its migration, the clump continuously accretes fresh gas and forms stars, increasing its stellar mass and decreasing its gas fraction and sSFR, even if the total gas mass and SFR do not change much. New generations of stars enrich the clump with metals, causing metallicity to increase during the migration. When the clump reaches the center at the end of its migration, its mass-weighted mean stellar age is of the order of the migration time, namely several hundred Myr. Thus, the clump ages are predicted to be between several tens and several hundreds of Myr and their masses should have a spread of about a factor of 3, with clumps nearer the galactic center being more massive and older, with lower gas fractions and sSFRs but higher metallicities.

This is in stark contrast to the expectations from Scenario II, where the stellar populations in the clumps do not have a chance to evolve much or develop such an age spread, as they are all recycled back into the disc within less than 100 Myr. Genel et al. (2012b) report that their simulated clump masses are all within a factor of 2 of each other, at the scale of the turbulent Jeans mass of the disc, with no clear gradient in the clump mass to distance relation. Their clumps do exhibit an age gradient, but this closely follows that of the inter-clump stars and is fairly shallow, with a logarithmic slope of -0.57 ± 0.14 , compared to -0.86 ± 0.03 in our simulations. Only $\sim 20\%$ of the stellar mass in their clumps was formed in the clump itself, the remaining 80% being background disc stars, while in the majority of our *in-situ* clumps, more than 50% of the clump mass consists of stars formed internally in the

clump. Since observations of high- z SFGs indeed reveal rather weak gradients in both color and mass-to-light ratios across the disc (Förster Schreiber et al. 2011a), the gradients in stellar age of disc stars are not expected to be very strong, and neither are the gradients of clump properties in scenario II.

In principle, we could imagine a stronger radial variation of clump age even in scenario II, if we allow the efficiency of clump formation to vary with radius. However, in this case we should still expect the age gradient for the clumps to be close to that of the background disc stars, because clumps only experience one major episode of star-formation before disrupting and depositing all their newly formed stars in the surrounding disc. This will cause the disc to appear younger in regions where clump formation/disruption is efficient, and somewhat older elsewhere, where few young clumps are found. The exact gradient of the disc age will then be determined by the ratio of the clump formation timescale to the migration timescale of the stars, but we can likely expect it to be steeper than what we see in our simulations, where the stellar disc age is nearly constant with radius, and to follow more closely the *in-situ* clump age gradient.

In order to distinguish between the two scenarios regarding the fate of the giant clumps, detailed observations of clump properties within the disc are needed. The dominant distinguishing feature between the two scenarios is the age spread among the clumps. Observations revealing spreads of more than 100 Myr would provide strong evidence against scenario II. A further test calls for detailed observations of the radial trends of clump properties within the disc. These should then be compared to the underlying gradients in the smooth disc component, to determine if the clumps evolved separately, indicating long lived stages of equilibrium. Since contamination by *ex-situ* clumps will tend to smooth the observed gradients if they are not separated from the *in-situ* clumps, any observed gradient in clump properties beyond that of the background disc may be considered a lower limit on the intrinsic gradient, and evidence against scenario II.

It is important to keep in mind that reality likely lies in between the two extreme scenarios outlined above. Future work examining simulations with more realistic feedback, as described in Ceverino et al. (2014), will determine how robust the various gradients are to steady outflows from clumps with mass loading factors of order unity, rather than $\eta \sim 0.3$ as in our current simulations. Recent results from isolated disc simulations incorporating radiative feedback (Bournaud et al. 2014) as well as analytic estimates (Dekel & Krumholz 2013) suggest that with realistic outflows, the mass gradient may be suppressed.

7.2 Comparison with Observations

We summarize here some of the main observational results concerning the giant clumps in high-redshift SFGs, and comment on their theoretical implications in view of our findings in the current paper. A list of relevant references includes Elmegreen et al. (2004b);

Elmegreen & Elmegreen (2005); Förster Schreiber et al. (2006); Genzel et al. (2008); Elmegreen et al. (2009); Förster Schreiber et al. (2011b); Jones et al. (2010); Genzel et al. (2011); Guo et al. (2012); Wuyts et al. (2012).

7.2.1 General Evidence for VDI

When "clump-cluster" and "chain" galaxies were first observed at $z = 1 - 2$ (Cowie et al. 1995; van den Bergh 1996), many believed them to be merging systems. However, studies of the distributions of shapes of such galaxies at $z = 1 - 3$ (Elmegreen et al. 2004a, 2005), followed by resolved kinematic studies of massive SFGs at $z \sim 2$ using integral field spectroscopy (Förster Schreiber et al. 2006, 2009; Genzel et al. 2006; Shapiro et al. 2008), revealed many of these systems to be extended rotating disc galaxies showing no signatures of major mergers. Toomre gravitational disc instability in its violent phase is an obvious alternative mechanism for the formation of the clumpy phase (e.g. DSC09 and references therein). Indeed, the observations indicated indirectly that these discs may be gravitationally unstable, with $Q \leq 1$ (e.g. Genzel et al. 2006, 2011), though it is hard to learn about the linear instability from the nonlinear conditions in the observed discs.

Estimates by Wuyts et al. (2012) of the overall fraction of clumpy discs at redshifts $z = 1.5 - 2.5$ range from $\sim 40 - 75\%$, depending on the band used to identify clumps. However, we note that in this study, clumps are not detected individually as in our work, but are rather defined as off-center pixels with heightened surface density in stacked, pixelated images of the galaxy population. Observations of a large sample of galaxies from the CANDELS survey, where clumps are detected both visually and using an automated algorithm similar in spirit to the one implemented in this work (Y. Guo et al., in preparation), reveal clumpy fractions of $\sim 40 - 60\%$ for galaxies in a similar mass and redshift range as studied in this work. Both these results are consistent with the clumpy fractions predicted by our simulations.

Subsequent estimates of the masses of clumps in the redshift range $z = 1 - 3$ reveal them to be one to a few percent of the disc mass each, consistent with Toomre instability theory, and altogether contributing 10-20% (Elmegreen & Elmegreen 2005; Elmegreen et al. 2009; Förster Schreiber et al. 2011b; Genzel et al. 2011; Guo et al. 2012; Wuyts et al. 2012). These same studies also find that the contribution of clumps to the total SFR in the disc is higher, roughly 10-20% individually and up to 40% altogether, though there is significant scatter. Wuyts et al. (2012) finds that not only do clumps contribute less to their host galaxy's mass than to their light, they also contribute more light in bluer wavelengths, indicative of younger stellar populations and active star formation. The results from our simulations share these general trends, though the simulated clump masses tend to be slightly below the observed values. This can be largely explained by

observational beam smearing causing the clumps to appear larger than they actually are (see section 6 in Ceverino et al. (2012), especially their figure 19). Combined with improper background and foreground subtraction, this raises the clumps' contribution to the disc mass and SFR. Taking this into account, the fractions we find are in agreement with the clump masses deduced from the observations.

7.2.2 *In-situ Clumps vs. Mergers*

We have learned that the populations of VDI *in-situ* clumps and merging *ex-situ* clumps are distinguishable. If the two populations are not properly separated, the testing of the theoretical predictions for the *in-situ* clumps in the competing scenarios may prove difficult, as the *ex-situ* clumps can have qualitatively different properties. Efforts must therefore be made to distinguish between the two populations observationally, rather than by dark-matter contrast as in this work. Our results suggest that any off-center clump containing more than $\gtrsim 10\%$ of the total disc mass, such as observed by (e.g.) Genzel et al. (2011), is likely to be an *ex-situ* clump, since such high mass *in-situ* clumps are rare. Another possible distinction relies on observing clumps close to the disc edge. If such a clump has a stellar population of age ~ 1 Gyr and a low sSFR $\sim 0.1 \text{ Gyr}^{-1}$, it is almost definitely an *ex-situ* clump. All the *in-situ* clumps at these large radii should be dominated by a young stellar population of $\lesssim 80$ Myr and have high sSFR $\sim 5 \text{ Gyr}^{-1}$. These differences become less pronounced at smaller radii.

In many cases, young stellar ages and high sSFRs and gas fractions should translate to observed blue colors and vice versa. However, realistic luminosities and

colors will depend on the effects of dust. In an ongoing work, dust and radiative transfer is incorporated into the simulated galaxies using the SUNRISE code, thus creating realistic mock observations comparable to CANDELS data (Moody et al. 2014). Preliminary results show that *in-situ* clumps are not affected much by dust near the disc edge in face-on images and they indeed tend to appear very blue, so the distinctions between *in-situ* and *ex-situ* discussed above should be observable. However, in edge on views and toward the central parts of the disc, the *in-situ* clumps are reddened, and the differences between the clump types become less pronounced.

Observations find most off-center clumps to be blue (Elmegreen & Elmegreen 2005; Förster Schreiber et al. 2011b; Guo et al. 2012; Wuyts et al. 2012). Based on our analysis of the simulations and the preliminary SUNRISE images, this suggests that the majority of the observed off-center clumps are, indeed, *in-situ* rather than *ex-situ* in origin. The observations also suggest that the off-center clumps are peaks in the distribution of sSFR, similar to what we find for the *in-situ* clumps, which have sSFR values a factor of ~ 5 higher than the median of the smooth disc.

A few of the observed off-center clumps are redder and more massive (Förster Schreiber et al. 2011b), and

these may well be *ex-situ* clumps. It is also possible that more *ex-situ* clumps have been observed, but classified as mergers rather than clumps. In addition, central massive red clumps have been observed (Elmegreen et al. 2009; Guo et al. 2012; Wuyts et al. 2012) which seem to resemble our *bulge* clumps.

Given the mounting theoretical and observational evidence that most of the high- z SFGs are extended discs undergoing VDI and that external mergers are responsible for only a part of the clump population, it would not make sense to classify the high- z SFGs using the familiar classification schemes used at low redshifts. In particular, the high- z VDI phase with giant clumps is unlikely and therefore unaccounted for at low redshift, where disc instability takes the form of a bar and spiral arms associated with secular evolution. This calls for a new classification scheme for high redshift galaxies, which recognizes the dominance of VDI systems and explicitly differentiates between VDI galaxies and merging systems. Such a scheme will be devised using the SUNRISE images of the simulated galaxies together with the complete merger history of all the clumps.

7.2.3 *Clump Survival: Scenario I vs. Scenario II*

The stellar ages of clumps and their predicted lifetimes are being estimated observationally, though with very large uncertainties. Elmegreen & Elmegreen (2005) observed ten clump-cluster galaxies in the HUDF at $1.6 < z < 3.0$ with 5-10 clumps each, and estimated clump ages of 100 – 800 Myr, with an average of 340 Myr, hosted in older discs of 1.4 – 3 Gyr. Then Elmegreen et al. (2009) found a very large range of ages for star-forming clumps, centered around 100 Myr but reaching values as high as 1 Gyr. Genzel et al. (2011), who examined five $z \sim 2.2$ clumpy SFGs with SINFONI, estimated clumps to be between 10 and a few hundred Myr old, with typical clumps having stellar ages of 100 – 200 Myr and an upper envelope of 300 Myr. Additional considerations led them to estimate the average lifetime of clumps to be ~ 500 Myr. Förster Schreiber et al. (2011b) obtained ages for 7 clumps in one galaxy from the SINS survey, which ranged from a few tens to about ~ 250 Myr, centered on just below 100 Myr. Wuyts et al. (2012) used a mass complete sample of 326 SFGs at $1.5 < z < 2.5$ and another 323 SFGs at $0.5 < z < 1.5$, pixelated and stacked the images and defined clumps as off-center pixels with elevated surface brightness above the background. At $z \sim 2$, the clump pixels have ages of ~ 200 Myr, far younger than the off-clump pixels. At $z \sim 1$, both the clumps and the discs are older by about a factor of 2. Guo et al. (2012) collected data on ~ 40 clumps from ten galaxies in the HUDF and found the distribution of clump ages to be roughly lognormal, centered on ~ 300 Myr, but covering a wide range from 10 Myr to a few Gyr, while the disc ages were concentrated in the range 0.3 – 1 Gyr.

These studies all use different methods for estimating the clump stellar ages, but all agree that the uncertainties of the models are very large. Nevertheless,

the fact that the clumps exhibit such a wide range of ages in any particular study and that even low estimates on clump ages are rarely far below 100 Myr seem to favour scenario I over scenario II. In other words, it appears that clumps are indeed able to survive for durations of several hundred Myr and do not disrupt on dynamical timescales of $\sim 50 - 100$ Myr.

Some of these studies (Förster Schreiber et al. 2011b; Guo et al. 2012) have even attempted to measure radial variations of clump properties within the discs. They find evidence for older, redder and more massive clumps to be located closer to the disc center. Förster Schreiber et al. (2011b) find a logarithmic slope for the ages of seven clumps in a single galaxy of -2.06 ± 0.63 , much steeper than the radial variation of the background disc. They note that even if the absolute values for clump ages are wrong, the relative trend should hold. In another galaxy from their sample, also containing seven clumps, they found clumps to become redder closer to the center, with increased mass-to-light ratios. Clumps near the disc edge have masses of $\sim 10^8 M_\odot$ while close to the center the masses are $\gtrsim 6 \times 10^8 M_\odot$. Guo et al. (2012) find that clumps closer to the disc center have lower sSFRs, older ages, higher dust extinctions and higher stellar surface densities. Moreover, they find the radial variation in clump properties steeper than the global gradients in the background disc, and deduce that the clumps must have evolved separately from the disc in a state of quasi-equilibrium. They find clumps within 0.1 times the disc radius to have sSFR values 5 times lower and stellar surface densities 25 times higher than clumps in the outer half of the disc, very similar to the results from our simulations of scenario I. The clumps near the disc center have ages of roughly 700 Myr as opposed to ~ 100 Myr in the outer disc. These studies, while crude and preliminary, are in good agreement with the predictions of clump migration in scenario I as simulated in the current paper, which seems to indicate that clumps survive for extended periods longer than an orbital time and evolve as they migrate inwards.

7.3 Co-rotation of *Ex-situ* Clumps

We found that roughly half the *ex-situ* clumps are co-rotating with their background in the disc, and some of their properties are systematically different from those *ex-situ* clumps with significant vertical or radial velocity components. The median masses and SFRs of the former are larger by factors of ~ 2 and ~ 25 respectively, their median gas fraction is ~ 3 times higher and their median sSFR is ~ 8 times higher.

The co-rotation and associated clump properties may partly be a result of the initial properties of the incoming satellite. The degree of co-rotation may correlate with the initial orbit of the incoming satellite, and with the time since it first hit the disc. It may also depend on the gas fraction in the incoming clump, as ram pressure could be the mechanism that forces the satellite to join the disc kinematics. Finally, it may correlate with the clump total mass, if the mechanism that brings the satellite into the disc is tidal torques or

dynamical friction. Indeed, the co-rotating clumps are distinguished by their higher total mass and gas mass. Perhaps even more important in producing the distinct properties of the co-rotating clumps are the later evolutionary effects within the disc. Once co-rotating for whatever reason, the clump would tend to migrate inwards like the *in-situ* clumps and to grow in mass by accretion of gas from the disc (§7.1). The fresh gas will naturally increase the SFR. The origin of the kinematics bimodality of the *ex-situ* clumps will be addressed using the simulations along these lines in a future work.

The kinematic bimodality of *ex-situ* clumps should be detected observationally. One can identify a subsample of *ex-situ* clumps by their distinct properties described in the previous subsection, and measure their kinematics with respect to the host disc. One can then search for systematic difference in mass, gas fraction, sSFR and position within the disc between the two kinematic subsamples.

7.4 Caveats and Future Prospects

We can mention 3 main caveats regarding our simulations. First, despite the high resolution that allows the clump analysis in the first place, it is limited to only marginally resolving the clumps and not accounting for their sub-structure. Ceverino et al. (2012) compared a small sample of clumps from the simulations described here to a few clumps from disc galaxies simulated in isolation with a varying resolution up to ~ 1 pc. The high-resolution clumps, showing a rich substructure, appear to have similar masses and sizes to those from our simulations, and they also remain in Jeans equilibrium while migrating towards the disc center. We therefore do not expect the resolution to have a major effect on the global properties of individual clumps. The effect of resolution on VDI and on the clump properties is being tested using a new suite of simulations with twice higher resolution (Moody et al. 2014; N. Mandelker et al., in preparation).

Second, as mentioned in §2, the SFR efficiency in a free-fall time as assumed in the current simulations led to an overestimate of the SFR at $z > 4$ and thus to an underestimate of the gas fraction and SFR at $z \sim 2$, by a factor of order two. It seems reasonable that underestimating the gas fraction may cause us to underestimate the importance of VDI and the degree of clumpiness in our discs, since these are mostly driven by the gas and young stars, thus making our studies of VDI at $z \sim 2$ rather conservative. This will be tested using a new suite of simulations with higher resolution and reduced star-formation efficiency.

Third is the fairly weak feedback incorporated in the current simulations, which helps the overestimate of SFR at very high z , and underestimates the effect of outflows on clump survival. This will be examined (N. Mandelker et al., in preparation) using a new suite of cosmological simulations (Ceverino et al. 2014) that employ stronger momentum-driven feedback, at a physically realistic level of a few times L/c (Dekel & Krumholz 2013). While a systematic study of outflows from clumps in our existing simulations has

not yet been performed, we note that a few individual cases of clumps exhibiting strong outflows have been identified. These clumps were found near the edge or outside the slim disc, where the ambient gas density is low. The outflows caused the clumps to lose most of their gas in less than 100 Myr. However, the stellar clump remained intact, and after reentering the slim disc, was observed to accrete fresh gas and continue its migration to the disc center.

There are several additional interesting issues concerning the clump properties that we will explore in future work. These include mutual correlations between different clump properties, and between the clump properties and the characteristics of the host galaxy. Both these topics are relevant for comparison with observations. A further avenue for future work involves tracking individual clumps through time in the simulations. Recall that in our current simulations, clumps may be present in the disc for 2-3 consecutive snapshots before completing their migration. During this time, they can be tracked based on their stellar particles and insight can be gained on their individual formation and evolution. Such a detailed analysis is currently being performed on clumps produced in our new simulations (A. Dekel, F. Bournaud and N. Mandelker, in preparation; N. Mandelker et al., in preparation). Preliminary results suggest that the frequency and longevity of clumps with baryonic masses $\gtrsim 10^8 M_\odot$ are unaffected by the inclusion of radiative feedback. The age gradient is still present and is only mildly suppressed compared to our current simulations. However, the mass gradient may be strongly suppressed, as outflows due to feedback can balance the inflow of gas from the disc onto the clumps, so the clump mass does not evolve much during migration. In addition, several simulations are being run with much denser time spacing between outputs to allow individual clumps to be followed more accurately.

Also interesting will be to address the validity and properties of VDI at very high $z > 3$ and low $z < 1$ redshifts. Pioneering observations of massive galaxies out to $z \sim 10$ may start exploring the extent to which VDI operates also earlier than $z \sim 3$. This question will be addressed using simulations in future work, where we will have to struggle with the limitation that only the most massive galaxies are properly resolved in our current simulations before $z \sim 4$. Preliminary visual inspection of the existing simulations do reveal at least a few cases of massive galaxies with a clumpy appearance already at $z \sim 5-6$. In order to address the fate of VDI at $z < 1$, and the low-redshift descendants of the VDI galaxies seen at $z \sim 2$, we will push the simulations to after $z \sim 1$.

The analysis presented here has been performed in 3D, taking full advantage of the information available in the simulations. While this method has helped us develop a theoretical understanding of VDI, one should now worry about how to directly compare our results with realistic 2D observations that also suffer from dust effects, background and foreground contamination, and beam smearing. As described in §7.2, efforts are being made to “observe” these simulated galaxies in a realistic

way, e.g. for comparison with CANDELS data. Using these “observed” simulated galaxies and their merger histories will allow the development of more accurate observable criteria for distinguishing between *in-situ* VDI clumps and merging clumps, and thus devise a new theory-motivated classification scheme for high- z galaxies, which explicitly accounts for VDI.

8 CONCLUSION

We have studied the properties of giant clumps in $1 < z < 4$ disc galaxies using a suite of high resolution hydro-cosmological simulations. The simulations used here, being characterized by moderate stellar feedback, may underestimate the outflow mass loss from clumps. The result may be an overestimate of the clump mass growth during its migration, but we expect most other clump properties to be recovered in a qualitatively robust way. Our main results can be summarised as follows:

(i) On average, $\sim 70\%$ of the discs host off-center clumps, while $\sim 60\%$ specifically host *in-situ* clumps, formed by VDI. The fraction of clumpy discs peaks at intermediate disc masses of $M_d \sim 10^{10.5} M_\odot$ at $z \lesssim 2$. Considering only the clumpy discs, there are on average 3.2 *in-situ* clumps per disc, together contributing 1-7% of the disc mass (with a median of 3-4%) and 5-45% of the disc SFR (with a maximal probability of 40% and a median of 22%). Considering only the discs undergoing VDI the average number of *in-situ* clumps per disc is 3.7.

(ii) Among the off-center clumps, *in-situ* clumps make up roughly 75% in number, $\lesssim 80\%$ in SFR and $\lesssim 50\%$ in baryonic mass. Individual *in-situ* clumps contain $\sim 1-2\%$ of the disc baryonic mass, in agreement with standard Toomre analysis. Their contribution to the disc SFR is greater, with individual clumps having $\sim 5-6\%$ of the disc total. They have high gas fractions, typically $\sim 10\%$, though the youngest clumps have more than 50%. As a result, they have high sSFRs, typically $\gtrsim 2 \text{ Gyr}^{-1}$, with the youngest clumps having sSFRs above 10 Gyr^{-1} . Their median stellar age is $\sim 160 \text{ Myr}$ with a broad peak at 150 – 300 Myr, and a sharp decline at older ages. This is comparable to 1-2 orbital times at the disc edge which is the expected migration time for clumps (DSC09). Typical metallicity values are $\log(O/H) + 12 \sim 8.9$, though the youngest, most actively star forming clumps still have sub-solar values. The *in-situ* clumps exhibit radial trends, where clumps closer to the disc center are more massive and have lower gas fractions, lower sSFR, older stellar ages and higher metallicity.

(iii) *Ex-situ* clumps, which joined the disc as minor mergers, were primarily identified by their dark matter contrast with respect to the host halo. The average number of *ex-situ* clumps per disc is 0.5 among all the discs, 0.7 among the clumpy discs, and 0.6 among the discs undergoing VDI. The *ex-situ* clumps turn out to be about 25% of all the off-center clumps in number, over 20% in SFR and more than 50% in

mass. A typical *ex-situ* clump contains about 4% of the disc mass, though it is not uncommon to find massive clumps having 10-30% of the disc mass. Their SFR is uncorrelated with the host disc, and the SFR distribution among the clumps is uniform in the range 0.001-1 times the total disc SFR. Their gas fractions are typically $\lesssim 1 - 3\%$, lower than the *in-situ* clumps, resulting in lower sSFR values of $\sim 0.25 \text{ Gyr}^{-1}$ and old stellar ages of order 1 Gyr. On the other hand, the metallicities are similar to those of the *in-situ* clumps, especially in the gas phase. The *ex-situ* clumps are more massive closer to the disc center, but show no significant radial trends in their other properties. The exception is a tendency for clumps interior to R_d to have higher gas fractions, SFRs and sSFRs than those outside R_d . Roughly half of the *ex-situ* clumps are co-rotating with their host disc, the remainder exhibiting large vertical or radial velocities. These co-rotating clumps typically have higher masses, SFRs, gas fractions and sSFR than the non-co-rotating ones, and they can have sub-solar metallicities similar to the *in-situ* clumps. This is consistent with accretion of fresh gas from the disc during migration inwards.

(iv) In addition to the off-center clumps, there is a compact *bulge* clump at the center of $\sim 91\%$ of our discs. These *bulge* clumps are typically smaller in size than the stellar bulge, representing gaseous overdensities at the bulge center. On average, *bulge* clumps have masses of $\sim 0.4M_d$, an order of magnitude more massive than a typical off-center clump. The SFR in the *bulge* clumps is typically $\sim 20\%$ of the disc value, a factor of $\lesssim 4$ higher than typical *in-situ* clumps. They typically have low gas fractions of less than 1%, low sSFR of $\sim 0.2 \text{ Gyr}^{-1}$, and old stellar populations with ages of order 1 Gyr. They are also metal rich with $\log(O/H) + 12 \sim 9.1 - 9.2$. At high redshifts they are often gas rich and star forming, with SFR values greater than the disc itself, resembling the observed "blue nuggets" (Barro et al. 2013; Dekel & Burkert 2014).

(v) The *ex-situ* merged galaxies and the *in-situ* clumps can be partly distinguished by their masses. For example, a clump that is as massive as 10% or more of the disc is almost certainly *ex-situ* in origin. Assuming the clumps are not severely reddened by dust, one can partly distinguish *ex-situ* from *in-situ* clumps based on color, especially in the outer parts of the disc. *In-situ* clumps are expected to be blue, due to their high sSFRs and their young stellar ages, while the *ex-situ* clumps should exhibit redder colors characteristic of older stars and low sSFR. Preliminary analysis using SUNRISE suggest that the clumps are not significantly affected by dust in face-on images of the disc near the edge.

(vi) If the clumps survive intact for a migration time they are expected to accrete gas from the surrounding disc and increase their mass during the migration. The accretion promotes additional star formation during the migration. If the accretion rate and SFR remain roughly constant, the gas fraction and sSFR will decrease as the clump migrates inwards, while the metallicity increases. This would imply that the accretion of gas from the disc does not grow near the disc center, possibly due to the strong gradient of gas fraction in the disc or

to the strong tidal field near the center. The gradient of *in-situ* clump masses within the disc is consistent with the accretion scenario, as is the age gradient which is too steep to be explained by the gradient in the background disc. Preliminary observations of such radial gradients in clump properties tend to favour the clump survival and migration picture, as they are not expected in models where clumps are short lived. Observed gradients are only lower limits on the intrinsic evolution of *in-situ* clumps, as the presence of *ex-situ* clumps may contaminate the signal, though this is not expected to be a strong effect in the inner disc. Detailed observations of radial variations of clump properties across a large sample of galactic discs, possibly taking care to remove *ex-situ* mergers on a statistical basis, are needed to properly address the question of the lifetime of observed giant clumps.

ACKNOWLEDGMENTS

We acknowledge stimulating discussions with Yicheng Guo. The simulations were performed in the astro cluster at HU, at the National Energy Research Scientific Computing Center (NERSC), Lawrence Berkeley National Laboratory, and at NASA Advanced Supercomputing (NAS) at NASA Ames Research Center. This work was partially supported by ISF grant 6/08, by GIF grant G-1052-104.7/2009, by a DIP grant, by NSF grant AST-1010033 and by MINECO grants AYA2012-31101, and AYA-2009-13875-C03-02. DC is a Juan de la Cierva fellow.

REFERENCES

- Agertz O., Teyssier R., Moore B., 2009, MNRAS, 397, L64
 Asplund M., Grevesse N., Sauval A. J., Scott P., 2009, ARA&A, 47, 481
 Barro G. et al., 2013, ApJ, 765, 104
 Behroozi P. S., Wechsler R. H., Conroy C., 2013, ApJ, 770, 57
 Bournaud F., Dekel A., Teyssier R., Cacciato M., Daddi E., Juneau S., Shankar F., 2011, ApJ, 741, L33
 Bournaud F., Elmegreen B. G., 2009, ApJ, 694, L158
 Bournaud F., Elmegreen B. G., Elmegreen D. M., 2007, ApJ, 670, 237
 Bournaud F. et al., 2012, ApJ, 757, 81
 Bournaud F. et al., 2014, ApJ, 780, 57
 Brinchmann J., Charlot S., White S. D. M., Tremonti C., Kauffmann G., Heckman T., Brinkmann J., 2004, MNRAS, 351, 1151
 Bryan G. L., Norman M. L., 1998, ApJ, 495, 80
 Cacciato M., Dekel A., Genel S., 2012, MNRAS, 421, 818
 Ceverino D., Dekel A., Bournaud F., 2010, MNRAS, 404, 2151
 Ceverino D., Dekel A., Mandelker N., Bournaud F., Burkert A., Genzel R., Primack J., 2012, MNRAS, 420, 3490
 Ceverino D., Klypin A., 2009, ApJ, 695, 292

- Ceverino D., Klypin A., Klimek E. S., Trujillo-Gomez S., Churchill C. W., Primack J., Dekel A., 2014, *MNRAS*, 442, 1545
- Cheung E. et al., 2012, *ApJ*, 760, 131
- Cowie L. L., Hu E. M., Songaila A., 1995, *AJ*, 110, 1576
- Cresci G., Hicks E. K. S., Genzel R., Schreiber N. M. F., Davies R., Bouché N., Buschkamp P., et al., 2009, *ApJ*, 697, 115
- Daddi E. et al., 2010, *ApJ*, 713, 686
- Dekel A. et al., 2009a, *Nature*, 457, 451
- Dekel A., Burkert A., 2014, *MNRAS*, 438, 1870
- Dekel A., Krumholz M. R., 2013, *MNRAS*, 432, 455
- Dekel A., Sari R., Ceverino D., 2009b, *ApJ*, 703, 785
- Dekel A., Silk J., 1986, *ApJ*, 303, 39
- Dekel A., Zolotov A., Tweed D., Cacciato M., Ceverino D., Primack J. R., 2013, *MNRAS*, 435, 999
- Elmegreen B. G., Bournaud F., Elmegreen D. M., 2008, *ApJ*, 688, 67
- Elmegreen B. G., Elmegreen D. M., 2005, *ApJ*, 627, 632
- Elmegreen B. G., Elmegreen D. M., Fernandez M. X., Lemonias J. J., 2009, *ApJ*, 692, 12
- Elmegreen D. M., Elmegreen B. G., Hirst A. C., 2004a, *ApJ*, 604, L21
- Elmegreen D. M., Elmegreen B. G., Ravindranath S., Coe D. A., 2007, *ApJ*, 658, 763
- Elmegreen D. M., Elmegreen B. G., Rubin D. S., Schaffer M. A., 2005, *ApJ*, 631, 85
- Elmegreen D. M., Elmegreen B. G., Sheets C. M., 2004b, *ApJ*, 603, 74
- Ferland G. J., Korista K. T., Verner D. A., Ferguson J. W., Kingdon J. B., Verner E. M., 1998, *PASP*, 110, 761
- Ferreras I., Silk J., 2002, *MNRAS*, 336, 1181
- Forbes J., Krumholz M., Burkert A., 2012, *ApJ*, 754, 48
- Forbes J. C., Krumholz M. R., Burkert A., Dekel A., 2014, *MNRAS*, 438, 1552
- Förster Schreiber N. M., Genzel R., Bouché N., Cresci G., Davies R., Buschkamp P., Shapiro K., et al., 2009, *ApJ*, 706, 1364
- Förster Schreiber N. M., Genzel R., Lehnert M. D., Bouché N., Verma A., Erb D. K., Shapley A. E., et al., 2006, *ApJ*, 645, 1062
- Förster Schreiber N. M., Shapley A. E., Erb D. K., Genzel R., Steidel C. C., Bouché N., Cresci G., Davies R., 2011a, *ApJ*, 731, 65
- Förster Schreiber N. M. et al., 2011b, *ApJ*, 739, 45
- Freundlich J. et al., 2013, *A&A*, 553, A130
- Gammie C. F., 2001, *ApJ*, 553, 174
- Genel S., Dekel A., Cacciato M., 2012a, *MNRAS*, 3466
- Genel S. et al., 2012b, *ApJ*, 745, 11
- Genzel R., Burkert A., Bouché N., Cresci G., Förster Schreiber N. M., Shapley A., Shapiro K., et al., 2008, *ApJ*, 687, 59
- Genzel R., Tacconi L. J., Eisenhauer F., Förster Schreiber N. M., Cimatti A., Daddi E., Bouché N., et al., 2006, *Nature*, 442, 786
- Genzel R., et al., 2011, *ApJ*, 733, 101
- Guo Q., White S., Li C., Boylan-Kolchin M., 2010, *MNRAS*, 404, 1111
- Guo Y., Giavalisco M., Ferguson H. C., Cassata P., Koekemoer A. M., 2012, *ApJ*, 757, 120
- Haardt F., Madau P., 1996, *ApJ*, 461, 20
- Hopkins P. F., Kereš D., Murray N., Quataert E., Hernquist L., 2012, *MNRAS*, 427, 968
- Immeli A., Samland M., Gerhard O., Westera P., 2004a, *A&A*, 413, 547
- Immeli A., Samland M., Westera P., Gerhard O., 2004b, *ApJ*, 611, 20
- Jones T. A., Swinbank A. M., Ellis R. S., Richard J., Stark D. P., 2010, *MNRAS*, 404, 1247
- Kennicutt, Jr. R. C., 1998, *ApJ*, 498, 541
- Komatsu E. et al., 2009, *ApJS*, 180, 330
- Kravtsov A. V., 2003, *ApJ*, 590, L1
- Kravtsov A. V., Klypin A. A., Khokhlov A. M., 1997, *ApJS*, 111, 73
- Krumholz M., Burkert A., 2010, *ApJ*, 724, 895
- Krumholz M. R., Dekel A., 2010, *MNRAS*, 406, 112
- Krumholz M. R., Dekel A., 2012, *ApJ*, 753, 16
- Krumholz M. R., Thompson T. A., 2012, *ApJ*, 760, 155
- Krumholz M. R., Thompson T. A., 2013, *MNRAS*, 434, 2329
- Martig M., Bournaud F., Teyssier R., Dekel A., 2009, *ApJ*, 707, 250
- Moody C. E., Guo Y., Mandelker N., Ceverino D., Mozena M., Koo D. C., Dekel A., Primack J., 2014, *arXiv:1405.5266*
- Moster B. P., Naab T., White S. D. M., 2013, *MNRAS*, 428, 3121
- Moster B. P., Somerville R. S., Maulbetsch C., van den Bosch F. C., Macciò A. V., Naab T., Oser L., 2010, *ApJ*, 710, 903
- Murray N., Quataert E., Thompson T. A., 2010, *ApJ*, 709, 191
- Neistein E., Dekel A., 2008, *MNRAS*, 388, 1792
- Newman S. F. et al., 2012, *ApJ*, 752, 111
- Noguchi M., 1999, *ApJ*, 514, 77
- Oppenheimer B. D., Davé R., 2006, *MNRAS*, 373, 1265
- Oppenheimer B. D., Davé R., 2008, *MNRAS*, 387, 577
- Pérez-González P. G. et al., 2008, *ApJ*, 675, 234
- Renaud F. et al., 2013, *MNRAS*, 436, 1836
- Saintonge A. et al., 2011, *MNRAS*, 415, 32
- Shapiro K. L. et al., 2008, *ApJ*, 682, 231
- Stark D. P., Swinbank A. M., Ellis R. S., Dye S., Smail I. R., Richard J., 2008, *Nature*, 455, 775
- Steidel C. C., Erb D. K., Shapley A. E., Pettini M., Reddy N., Bogosavljević M., Rudie G. C., Rakic O., 2010, *ApJ*, 717, 289
- Tacconi L. J., Genzel R., Neri R., Cox P., Cooper M. C., Shapiro K., Bolatto A., et al., 2010, *Nature*, 463, 781
- Tacconi L. J., Genzel R., Smail I., Neri R., Chapman S. C., Ivison R. J., Blain A., et al., 2008, *ApJ*, 680, 246
- Tacconi L. J. et al., 2013, *ApJ*, 768, 74
- Toomre A., 1964, *ApJ*, 139, 1217
- van den Bergh S., 1996, *AJ*, 112, 2634
- Wisnioski E., Glazebrook K., Blake C., Poole G. B., Green A. W., Wyder T., Martin C., 2012, *MNRAS*, 422, 3339
- Woolsey S. E., Weaver T. A., 1995, *ApJS*, 101, 181

Wuyts S. et al., 2012, ApJ, 753, 114

APPENDIX A: COSMOLOGICAL SIMULATIONS WITH THE ART CODE

The cosmological simulations utilize the ART code (Kravtsov et al. 1997; Kravtsov 2003), which accurately follows the evolution of a gravitating N-body system and the Eulerian gas dynamics using an adaptive mesh refinement approach. Beyond gravity and hydrodynamics, the code incorporates many of the physical processes relevant for galaxy formation, as described in Ceverino & Klypin (2009) and in Ceverino et al. (2010). These processes, representing subgrid physics, include gas cooling by atomic hydrogen and helium, metal and molecular hydrogen cooling, and photoionization heating by a UV background, with partial self-shielding. Cooling and heating rates are tabulated for a given gas density, temperature, metallicity and UV background based on the CLOUDY code (Ferland et al. 1998), assuming a slab of thickness 1 kpc. A uniform UV background based on the redshift-dependent Haardt & Madau (1996) model is assumed, except at gas densities higher than 0.1 cm^{-3} , where a substantially suppressed UV background is used ($5.9 \times 10^{26} \text{ ergs}^{-1} \text{ cm}^{-2} \text{ Hz}^{-1}$) in order to mimic the partial self-shielding of dense gas. This allows the dense gas to cool down to temperatures of $\sim 300\text{K}$. The assumed equation of state is that of an ideal mono-atomic gas. Artificial fragmentation on the cell size is prevented by introducing a pressure floor, which ensures that the Jeans scale is resolved by at least 7 cells (see Ceverino et al. (2010)).

Star formation is assumed to occur at densities above a threshold of 1 cm^{-3} and at temperatures below 10^4K . More than 90% of the stars form at temperatures well below 10^3K , and more than half the stars form at 300 K in cells where the gas density is higher than 10 cm^{-3} . The code implements a stochastic star-formation model that yields a star-formation efficiency per free-fall time of 5%. At the given resolution, this efficiency roughly mimics the empirical Kennicutt law (Kennicutt 1998). The code incorporates a thermal stellar feedback model, in which the combined energy from stellar winds and supernova explosions is released as a constant heating rate over 40 Myr following star formation, the typical age of the lightest star that explodes as a type-II supernova. The heating rate due to feedback may or may not overcome the cooling rate, depending on the gas conditions in the star-forming regions (Dekel & Silk 1986; Ceverino & Klypin 2009). No shutdown of cooling is implemented. We also include the effect of runaway stars by assigning a velocity kick of $\sim 10 \text{ km s}^{-1}$ to 30% of the newly formed stellar particles. The code also includes the later effects of type-Ia supernova and stellar mass loss, and it follows the metal enrichment of the ISM.

The selected halos were drawn from an N-body simulation. The initial conditions corresponding to each of the selected haloes were filled with gas and refined to much higher resolution on an adaptive mesh within the

Lagrangian volume that encompasses the mass within twice the virial radius at the redshift when the halo was selected ($z = 0$ for MW6-MW9, $z = 1$ for the remaining halos). This is roughly a sphere of comoving radius 1 Mpc, and it was embedded in a comoving cosmological box with length ranging from $20 - 80 h^{-1} \text{ Mpc}$.

Table A1 summarizes the properties of our simulated halos, including the target halo mass, final redshift and virial properties at $z = 2$. Note that the most massive galaxy in our sample, MW5, did not reach redshift 2, so its virial properties are given at $z = 2.23$ when the simulation was stopped. The halo virial radius, R_v , is defined as the radius of a sphere within which the average density is a factor Δ_c times the universal mean. The overdensity is given by Bryan & Norman (1998) as:

$$\Delta_c = 18\pi^2 - 82x - 39x^2, \quad x \equiv 1 - \Omega(z) \quad (\text{A1})$$

A standard ΛCDM cosmology has been assumed, with the WMAP5 cosmological parameters $\Omega_m = 0.27$, $\Omega_\Lambda = 0.73$, $\Omega_b = 0.045$, $h = 0.7$ and $\sigma_8 = 0.82$ (Komatsu et al. 2009). The zoom-in regions have been simulated with $\sim (4 - 24) \times 10^6$ dark-matter particles of mass $6.6 \times 10^5 M_\odot$ each, and the particles representing stars have a minimum mass of $10^4 M_\odot$. Each galaxy has been evolved forward in time with the full hydro ART and subgrid physics on an adaptive comoving mesh refined in the dense regions to cells of minimum size 35-70 pc in physical units at all times.

Each AMR cell is refined to 8 cells once it contains a mass in stars and dark matter higher than $2 \times 10^6 M_\odot$, equivalent to 3 dark-matter particles, or it contains a gas mass higher than $1.5 \times 10^6 M_\odot$. This quasi-Lagrangian strategy ends at the highest level of refinement that marks the minimum cell size at each redshift. In particular, the minimum cell size is set to 35 pc in physical units at expansion factor $a = 0.16$ ($z = 5.25$), but due to the expansion of the whole mesh while the refinement level remains fixed, the minimum cell size grows in physical units and becomes 70 pc by $a = 0.32$ ($z = 2.125$). At this time we add a new level to the comoving mesh, so the minimum cell size becomes 35 pc again, and so on. This maximum resolution is valid in particular throughout the cold discs and dense clumps, allowing cooling to $\sim 300\text{K}$ and gas densities of $\sim 10^3 \text{ cm}^{-3}$.

APPENDIX B: DEFINING THE DISC FRAME

As described in the text, we model the discs as cylinders with radius R_d and height H_d (total thickness $2H_d$). We describe here how the disc plane and dimensions are determined.

We begin by iteratively defining the disc center. The initial estimate of the center is at the minimum of the potential well. This is then refined by computing the center of mass for the stars in spheres of decreasing radii from $r_{max} = 600 \text{ pc}$ to $r_{min} = 130 \text{ pc}$. After each iteration, we update the center and decrease the radius by a factor of 1.1. The algorithm stops once the radius gets below r_{min} or the number of stars in the sphere

Table A1. Properties of our 29 dark matter halos. The box sizes are in $h^{-1}\text{Mpc}$. *Target* M_v refers to the virial mass at the target redshift of the selected halo from the low resolution N-body simulation and is given in units of $10^{11}M_\odot$. The halos were selected at $z = 1$, except for MW6-MW9, which were selected at $z = 0$. z_f is the final redshift that the simulation reached. The virial properties are given at $z = 2$, except for MW5, for which they are given at $z = 2.23$ where the simulation was stopped. The virial mass is given in units of $10^{11}M_\odot$, the virial radius in units of kpc and the velocities in km s^{-1} .

<i>Gal</i>	<i>Box Size</i> $h^{-1}\text{Mpc}$	<i>Target</i> M_v $10^{11}M_\odot$	z_f	M_v $10^{11}M_\odot$	R_v kpc	V_v km s^{-1}
MW01	20	15.3	1.38	8.1	101.6	185.2
MW02	20	12.1	1.94	8.9	104.9	190.5
MW03	20	19.3	1.38	7.3	98.7	178.4
MW04	40	40.1	1.38	14.2	122.9	222.9
MW05	80	103.7	2.23	35.0	155.5	311.2
MW06	40	40.9	0.00	9.2	106.0	192.9
MW07	40	17.0	0.33	3.0	73.3	133.4
MW08	40	14.1	0.35	2.8	71.2	129.4
MW09	40	11.0	0.00	1.6	59.4	108.0
MW10	20	15.3	1.00	8.2	101.8	185.6
MW11	20	14.2	1.50	5.3	88.4	161.2
MW12	20	16.9	1.08	17.0	130.0	237.2
VL01	40	20.0	1.00	12.3	117.1	212.2
VL02	40	20.0	0.96	8.1	101.4	184.9
VL03	40	20.4	1.00	11.9	115.8	209.8
VL04	40	20.6	0.96	10.1	109.2	199.5
VL05	40	20.0	0.92	12.8	118.2	215.4
VL06	40	20.1	1.00	7.5	99.2	180.5
VL07	80	26.1	1.85	16.6	129.0	235.4
VL08	80	26.6	1.22	10.9	111.8	204.9
VL09	80	25.9	1.93	4.9	85.8	155.9
VL10	80	25.9	1.08	8.1	101.5	185.6
VL11	80	26.4	1.00	17.2	130.1	238.7
VL12	80	26.1	1.00	9.0	104.7	191.9
SFG1	40	33.0	1.17	16.6	128.7	235.3
SFG4	40	32.9	1.38	10.9	112.3	204.3
SFG5	40	33.3	1.00	13.8	123.0	219.6
SFG8	80	65.9	1.86	13.8	121.1	221.5
SFG9	80	51.7	1.03	18.9	134.8	245.3

drops below 20. A visual inspection of each snapshot was performed to ensure the correctness of the center.

We then proceed to determining the disc rest frame, axes and dimensions. Here we limit ourselves to cold gas with temperature $T < 1.5 \times 10^4 \text{K}$. This cut in temperature is important especially for calculating the angular momentum because while the warm / hot gas may have relatively little mass, it can have extremely high velocities and need not be co-rotating with the disc (e.g. gas escaping the disc as a result of feedback). All the cold gas, on the other hand, is assumed to have settled into a rotating disc. Our adopted temperature threshold must remove the non-co-rotating gas, while not removing too much of the disc mass. 10^4K is near the peak of the cooling curve for neutral atomic Hydrogen. The numerical factor 1.5 was determined by examining cumulative mass profiles of the gas in our simulated galaxies as a function of maximum temperature. For each galaxy, we calculated the fraction of mass in gas having $T < T_{max}$ compared to the total gas mass of the disc. The results are displayed in Fig. B1. On average, we find that $\sim 97\%$ of the gas

in the discs has $T < 1.5 \times 10^4 \text{K}$. The median remains roughly constant up to at least $5 \times 10^4 \text{K}$. This result is fairly insensitive to the exact dimensions of the cylinder within which we compute the mass ($r \leq R_d, 2R_d$; $|z| \leq H_d, 2H_d, 1 \text{kpc}$).

Using the cold gas, we iteratively compute the disc rest frame velocity \vec{v}_{cm} , angular momentum \vec{j}_d , radius R_d and height H_d . Our initial estimate for R_d is the half mass radius of the cold gas within a sphere of radius $0.15R_v$. The disc rest frame velocity, \vec{v}_{cm} , is then taken to be the center of mass velocity of cold gas within a sphere of radius R_d and the angular momentum of cold gas in this sphere, computed in the rest frame, defines the disc axis \hat{z}' . At this stage we initialize $H_d = R_d$.

The disc axis and dimensions are now refined, explicitly taking into account the cylindrical geometry of the disc. The procedure is as follows:

- (i) Rotate to the frame defined by \hat{z}' and examine the cylinder with radius $r = 0.15R_v$ and height $h = \min(H_d, 1 \text{kpc})$ (total thickness $2h$). Define the disc radius R_d as the radius which contains 85% of the cold gas mass in this cylinder.

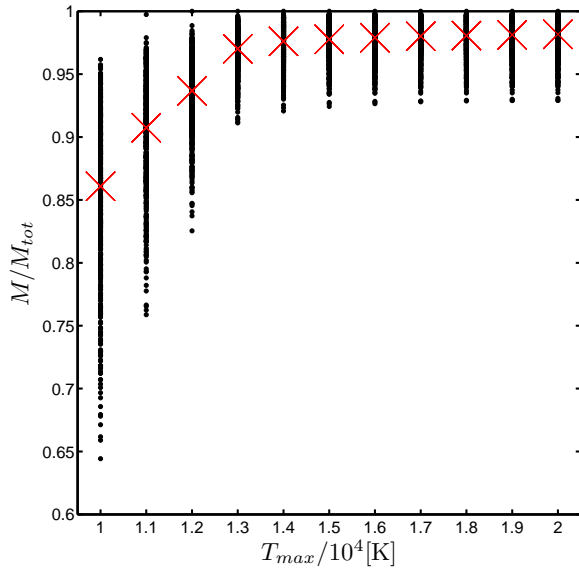


Figure B1. Temperature threshold for cold gas. Mass in gas with $T < T_{max}$ relative to the total gas mass contained within the disc ($r < R_d, |z| < H_d$), as a function of T_{max} . Black dots represent individual galaxies, while red crosses represent the medians. On average, $\sim 97\%$ of the gas has $T < 1.5 \times 10^4 \text{K}$.

(ii) Examine a cylinder where both the radius and the height are $r = h = R_d$. Define the disc thickness $2H_d$ as containing 85% of the cold gas mass within this cylinder.

(iii) Update \vec{v}_{cm} and \hat{z}' within the cylinder defined by R_d and H_d .

(iv) Repeat steps (i)-(iii) until R_d , H_d and \hat{z}' all converge to within 5%.

Convergence is usually achieved in 3-4 iterations, and in any case the process is stopped after 5 iterations (not including the initial spherical one).

To summarize, after the iterations have completed, the disc axis \hat{z}' is aligned with the angular momentum of cold gas ($T < 1.5 \times 10^4 \text{K}$) within a cylinder of radius R_d and height H_d . R_d contains 85% of the cold gas mass in a cylinder having radius $r = 0.15R_v$ and height $h = \min(H_d, 1 \text{kpc})$. The thickness of the disc contains 85% of the cold gas mass in a cylinder with both radius and height $r = h = R_d$.

The 3 axes in the disc frame are defined as follows:

$$\hat{z}' = \sin(\theta)\cos(\phi)\hat{x} + \sin(\theta)\sin(\phi)\hat{y} + \cos(\theta)\hat{z} \quad (\text{B1})$$

$$\hat{x}' = \cos(\theta)\cos(\phi)\hat{x} + \cos(\theta)\sin(\phi)\hat{y} - \sin(\theta)\hat{z} \quad (\text{B2})$$

$$\hat{y}' = -\sin(\phi)\hat{x} + \cos(\phi)\hat{y} \quad (\text{B3})$$

where \hat{x} , \hat{y} and \hat{z} are the three unit vectors in the simulation box frame and θ and ϕ are the standard polar and azimuthal angles. Note that \hat{z}' is aligned with the disc angular momentum, and the set $\hat{x}', \hat{y}', \hat{z}'$ form a right hand basis.

Figure B2 shows an example of the disc frame and dimensions for one of the galaxies in our sample: MW3 at expansion factor $a = 0.30$ (redshift $z \simeq 2.33$),

(Fig. 3). The radius and height for this galaxy are $R_d = 5.3 \text{kpc}$ and $H_d = 1.1 \text{kpc}$. In the figure we examine a box of dimensions $\pm 2R_d \times \pm 2R_d \times \pm 2H_d$ around the disc center, which is the volume probed for clumps in our analysis (§2.3).

APPENDIX C: IDENTIFYING GAS CLUMPS IN 3-D

In what follows we present in detail our method for detecting clumps in the simulations. The method is based on a two level smoothing of the 3D gas density field, first with a narrow gaussian of Full Width at Half Maximum (FWHM) $F_N = 140 \text{pc}$ and then with a wide gaussian of FWHM $F_W = 2 \text{kpc}$. Recalling that the maximal AMR resolution in our simulations is between 35 – 70 pc at all times, we see that F_N is always between 2 and 4 spatial resolution elements (or 1-2 force resolution elements) and serves only to wash out noise at the resolution level, having no serious effect on our results. The purpose of the wide gaussian is to approximate the large scale disc background and wash out any clumps. Observations which have attempted to directly estimate the sizes of high- z giant clumps suggest that the largest of them have diameters of $\sim 2 \text{kpc}$ (Förster Schreiber et al. 2011b; Genzel et al. 2011; Wisnioski et al. 2012), while numerical studies of clump properties in cosmological simulations indicate that clump diameters are even smaller (e.g. Ceverino et al. 2012; Genel et al. 2012b). Therefore, while our value for F_W is somewhat arbitrary, it should be a good estimate for our purposes. We have experimented with varying the value of F_W in the range 1.5–3 kpc and found the properties of *compact* clumps to vary at the $\sim 30\%$ level, while the sizes and masses of *diffuse* or elongated perturbations may vary by a factor of ~ 2 .

Using the two smoothed density fields, ρ_N and ρ_W respectively, we define the density residual $\delta_\rho = \frac{\rho_N - \rho_W}{\rho_W}$ and zero out all cells having $\delta_\rho < \delta_\rho^{\min} = 15$. The selected value for δ_ρ^{\min} depends on the selected value for F_W . Based on experimentation and visual inspection of ~ 20 snapshots from our sample, we found our adopted values to work well with each other and adopted them for all galaxies. Our objective was on the one hand to be able to detect all the clumps, even those with relatively low density contrast, but on the other hand to avoid situations where neighboring clumps were grouped together or where a clump was "buried" in an extended transient feature.

Neighbouring cells having $\delta_\rho > \delta_\rho^{\min}$ are grouped together and the cell with maximal ρ_N within each group defines the center. We assign a radius to each group, defined as the radius of a sphere containing 90% of the group mass. For groups which are roughly spherical, this provides a good estimate of their size, while for more elongated or filamentary ones it is not terribly meaningful. It must be stressed that while we do *not* strictly impose spherical geometry on our clumps but rather adhere to their identified shape, we

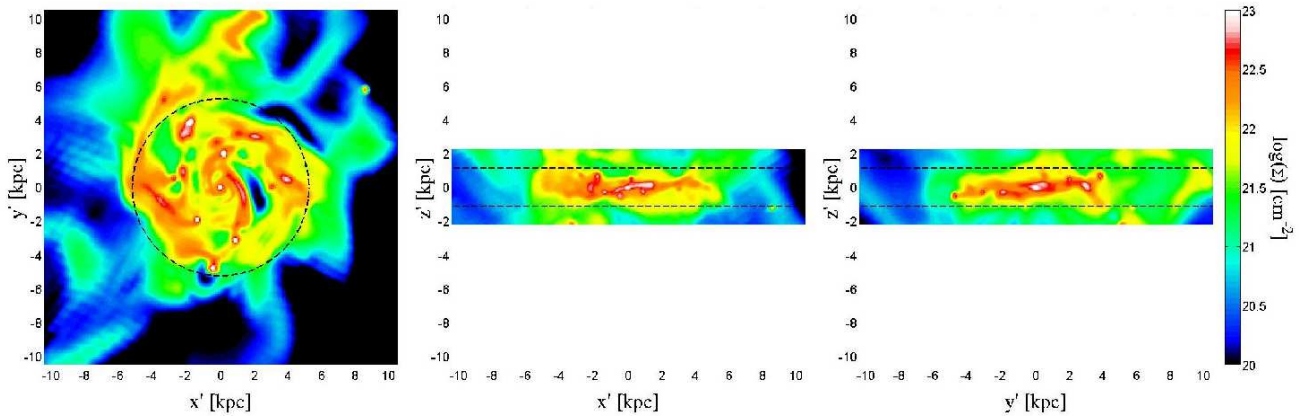


Figure B2. Disc frame. Face on and edge on views of one of our studied galaxies, MW3 at expansion factor $a = 0.30$ (redshift $z \simeq 2.33$). The axes are marked x', y' and z' in accordance with eq. (B1) - eq. (B3). In the face on view, the dashed circle marks the disc radius at $R_d = 5.3$ kpc, and in the two edge on views, the horizontal dashed lines mark the disc thickness at $z' = \pm H_d = \pm 1.1$ kpc. The face on image has been integrated over $\pm 2H_d$ and the two edge on images have been integrated over $\pm 2R_d$. The automated algorithm agrees well with the visual impression.

do remove from them any material lying outside this radius.

The final step involves applying a cut both in mass and in size. We impose a minimum volume for clumps of $F_N^3 = (140 \text{ pc})^3$. Our mass cut is *baryonic*, so we first add the stellar data onto the same grid used for the gas and compute the total baryonic mass for each identified group. We remove all groups with mass less than $10^{-4}M_d$, where M_d is the baryonic mass of the host disc. Note that this mass cut is very low, and does not affect any of our results, since all the compact, spherical clumps used in our analysis have masses $\gtrsim 10^{-3}M_d$ (Fig. 10). Groups that pass both the volume and mass thresholds define our sample of clumps.

APPENDIX D: MARGINAL MASS AND REDSHIFT DEPENDENCE OF DISC CLUMPINESS

In §4 we addressed the distribution of discs in terms of their off-center clumpiness properties. In this section, we attempt to examine a possible dependence of the disc clumpiness on disc mass and redshift. We restrict our analysis here to discs with masses $\log(M_d) > 9.5$ and only account for clumps more massive than $0.01M_d$. Observations of high redshift clumpy galaxies are not expected to be sensitive to clumps below this mass ratio (Y. Guo, private communication). By limiting, as we have, the mass range of the discs examined, we should have a fairly complete sample of clumps, eliminating the bias caused by the simulation resolution. However, we caution that in the low mass discs the number of clumps may be subject to the resolution threshold.

We have divided our sample into three redshift bins, as shown in Fig. D1. For each bin, we show as a function of disc mass the fraction of clumpy discs, mean number of clumps per disc, mean contribution of clumps to the

disc baryonic mass and mean contribution of clumps to the total disc SFR. We do this separately for all off-center clumps and for *in-situ* clumps only. We have separately divided our sample into three bins of disc mass, and show the same four clumpiness properties as a function of redshift in Fig. D1. In both figures, we consider only bins that contain at least 10 galaxies.

At all redshifts, the fraction of clumpy discs is highest among intermediate mass discs with $\log(M_d) \sim 10.5$. This remains true if considering all off-center clumps or only *in-situ* clumps, and is also seen in preliminary CANDELS observations at $z < 3$ (Y. Guo et al, in preparation; M. Mozenna et al., in preparation). For high mass discs, the clumpy fraction appears to increase with time, also consistent with CANDELS observations. For intermediate mass discs, the clumpy fraction is higher at $1 < z < 2.5$ than at $2.5 < z < 4$ and reaches a maximum at $z \sim 2 - 2.5$, the origin of which is unclear at this time. The clumpy fraction is high as well at $3.5 < z$, though this is due primarily to *ex-situ* mergers and is not evident when examining only *in-situ* clumps. The clumpy fraction of low mass discs shows no apparent trend with redshift when examining all off-center clumps, also consistent with CANDELS data, though there may be a very marginal trend for increased clumpy fraction at $1 < z < 2$ when examining *in-situ* clumps only. If real, this may suggest an increase in the prevalence of VDI at lower redshifts for all masses. We also note that at $z < 2.5$, the intermediate mass discs appear to have the highest clumpy fraction.

The number of clumps per disc is perhaps the least certain statistic, due to the limitations of the simulation resolution. We note no significant trend with redshift for low mass discs or high mass discs. Intermediate mass discs contain more clumps on average at higher redshifts, due mainly to the higher frequency of *ex-situ* clumps. It also appears that lower mass discs contain

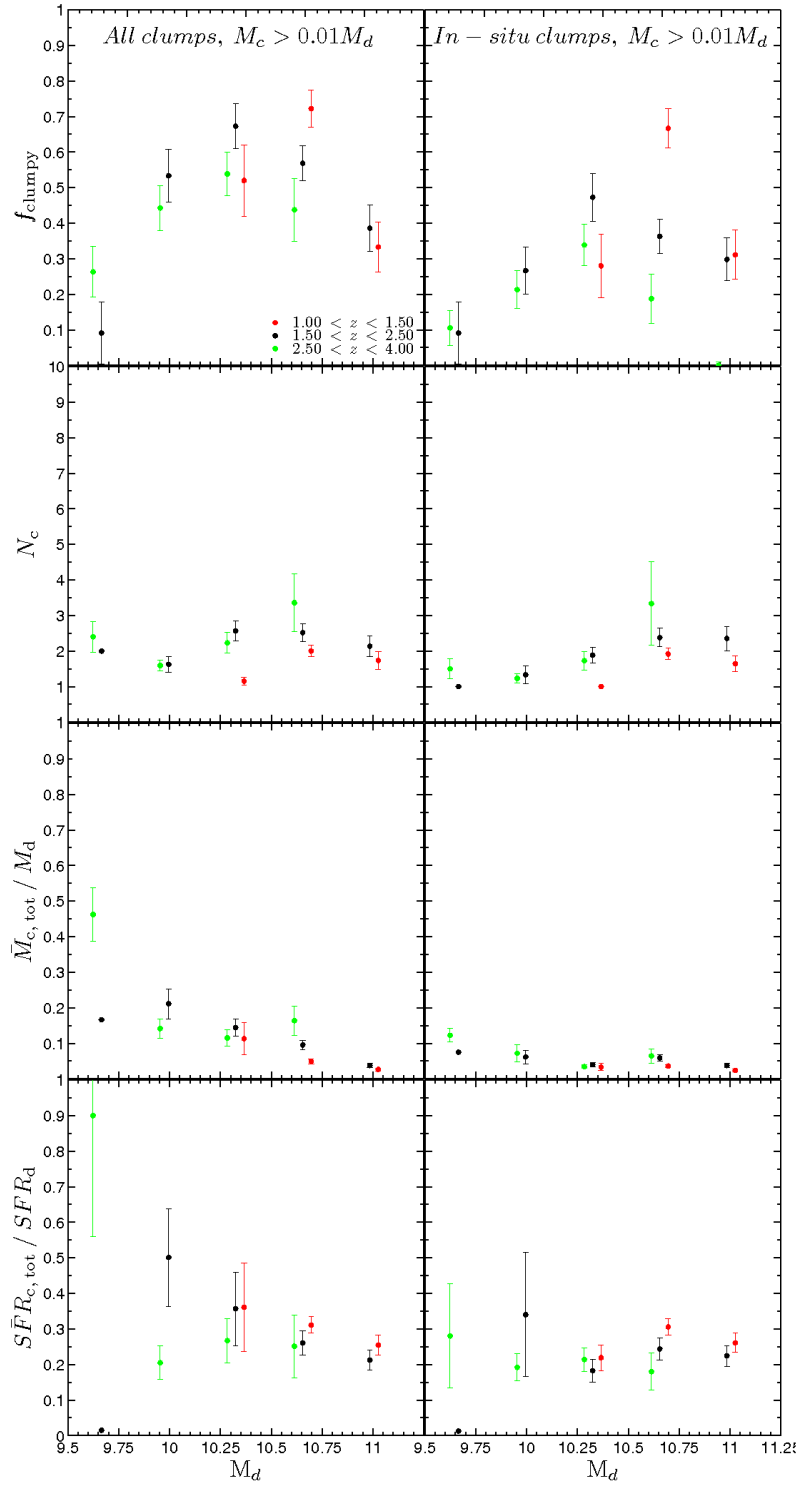


Figure D1. Clumpiness properties of our sample of discs as a function of disc mass and redshift. Discs are divided into three redshift bins: $2.5 < z < 4.0$, green; $1.5 < z < 2.5$, black; $1.0 < z < 1.5$, red; and their properties are plotted as a function of mass in 5 equally spaced bins from $9.5 < \log(M_d) < 11.25$. Only clumps with $M_c > 0.01 M_d$ were considered. Left panels consider all off-center clumps while right panels consider only *in-situ* clumps. **Top row:** Fraction of clumpy discs. Error bars mark 68% confidence levels of the standard error of percentage. **Second row:** Average number of clumps per disc, only for those discs with at least one clump. Error bars mark the standard error of the mean. **Third row:** Average contribution of clumps to the disc baryonic mass, only for those discs with at least one clump. Error bars mark the standard error of the mean. **Bottom row:** Average contribution of clumps to the total disc SFR, only for those discs with at least one clump. Error bars mark the standard error of the mean. The clumpy fraction peaks for intermediate mass discs. *In-situ* clumps contribute equally to disc mass and SFR at all disc masses.

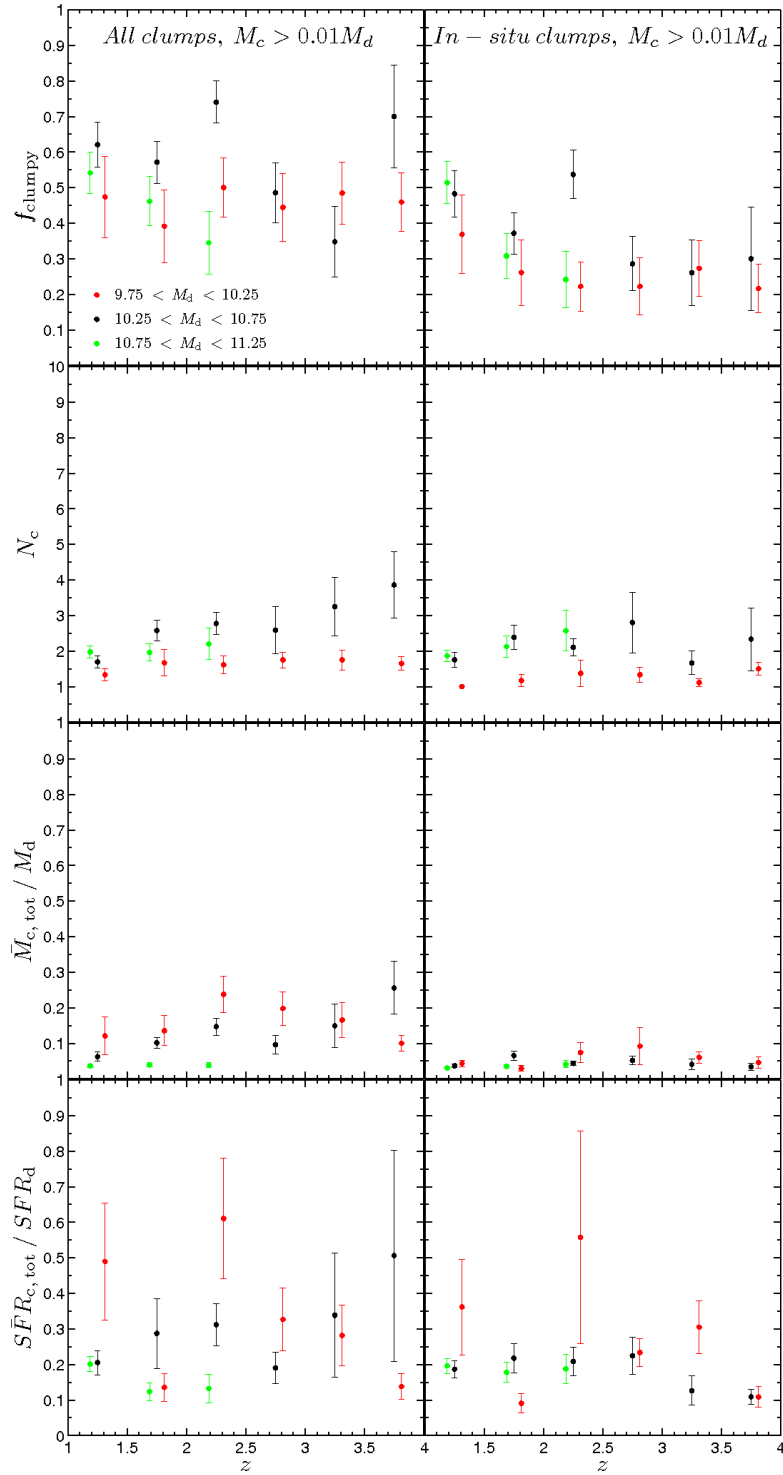


Figure D2. Clumpiness properties of our sample of discs as a function of disc mass and redshift. Discs are divided into three mass bins: high mass ($10.75 < \log(M_d) < 11.25$, green diamonds), intermediate mass ($10.25 < \log(M_d) < 10.75$, black circles) and low mass ($9.75 < \log(M_d) < 10.25$, red squares) and their properties are plotted as a function of redshift in 6 bins from $1 < z < 4$ with $\Delta z = 0.5$. Only clumps with $M_c > 0.01 M_d$ were considered. Rows, columns and error bars are as in Fig. D1. More discs appear clumpy at lower redshift, though the total mass and SFR in *in-situ* clumps does not seem to vary much.

fewer clumps on average, though this may well be an artifact of the resolution.

The most robust statistic is the contribution of clumps to the total disc mass, as this will be dominated by the most massive, well resolved clumps. Examining only the *in-situ* clumps, there does not appear to be any trend with disc mass or redshift, suggesting that during VDI, the disc will turn a constant fraction of its mass into clumps, $\sim 5-10\%$. *Ex-situ* clumps contribute more to the disc mass at $2 < z$, consistent with the theoretical estimate that the timescale for mergers of a given mass ratio, in terms of the galaxy dynamical time, is shorter at higher redshift (Neistein & Dekel 2008).

Finally, the contribution of clumps to the disc SFR appears highest for low mass discs. We note, however, that including less massive clumps with $M_c < 0.01M_d$ significantly weakens this trend. Therefore, we cannot draw any significant conclusions at this time. No additional systematic trends with disc mass or redshift are evident.

APPENDIX E: MEASURING OXYGEN FRACTIONS IN THE SIMULATIONS

Our simulations track the mass fraction in metals released from type Ia SNae (z_{SNIa}) and from type II SNae (z_{SNII}). These values are given for the gas as well as for the stellar particles. The metallicity values quoted in the text are in units of $\log(\text{O}/\text{H}) + 12$, where O/H is the ratio of Oxygen to Hydrogen atoms. This ratio is defined as

$$\frac{\text{O}}{\text{H}} = \frac{z_{\text{SNIa}} \cdot f_{\text{O,SNIa}} + z_{\text{SNII}} \cdot f_{\text{O,SNII}}}{X \cdot A_{\text{O}}} \quad (\text{E1})$$

where $f_{\text{O,SNIa}}$ and $f_{\text{O,SNII}}$ are the mass fraction of Oxygen in a typical SNIa and SNII explosion, respectively; X is the primordial abundance of Hydrogen and A_{O} is the atomic weight of Oxygen. Since all our galaxies are star forming galaxies with mean stellar ages $\lesssim 1$ Gyr, we obtain $z_{\text{SNIa}} \ll z_{\text{SNII}}$ (as predicted by Ferreras & Silk (2002)). Moreover, since the typical ratio of α nucleotides to Fe elements in SNII explosions is ~ 30 (Ferreras & Silk 2002), we take $f_{\text{O,SNII}}$ to be the mass fraction of Oxygen relative to α nucleotides in SNII explosions. We adopt a value of $f_{\text{O,SNII}} = 0.5$ based on Woosley & Weaver (1995). The atomic weight of Oxygen is $A_{\text{O}} = 16$ and we adopt $X = 0.755$. Thus, the final formula is:

$$\frac{\text{O}}{\text{H}} = 0.5 \frac{z_{\text{SNII}}}{0.755 \cdot 16} \quad (\text{E2})$$

This paper has been typeset from a $\text{T}_{\text{E}}\text{X}/\text{L}^{\text{A}}\text{T}_{\text{E}}\text{X}$ file prepared by the author.